

Interaction Between Mineralization and Rock Magnetization: New Constraints From a Silurian-Lower Devonian Volcanogenic Massive Sulfide (VMS) Deposit

Xinwei Hu^{1,2} , Liang Gao^{1,2,3} , Qingfei Wang^{1,2} , Shihong Zhang^{1,2} , Xiang Sun^{1,2} , Shengchao Xue^{1,2}, Xin Tang^{1,2}, Zhenyu Yang⁴ , and Jun Deng^{1,2} 

¹State Key Laboratory of Geological Processes and Mineral Resources, China University of Geosciences, Beijing, China,

²Key Laboratory of Marine Mineral Resources and Polar Geology (China University of Geosciences, Beijing), Ministry of Education, Beijing, China, ³School of Ocean Sciences, China University of Geosciences, Beijing, China, ⁴College of Resources, Environment and Tourism, Capital Normal University, Beijing, China

Key Points:

- Magnetite is the major magnetic carrier of hydrothermally altered surrounding rocks and orebodies
- Magnetite consumption occurred from chloritization via silicification to mineralization
- Rock magnetism reveals the neoformation of superparamagnetic and single domain magnetite during chloritization and illitization, respectively

Supporting Information:

Supporting Information may be found in the online version of this article.

Correspondence to:

L. Gao and J. Deng,
lgao@live.cn;
djun@cugb.edu.cn

Citation:

Hu, X., Gao, L., Wang, Q., Zhang, S., Sun, X., Xue, S., et al. (2023). Interaction between mineralization and rock magnetization: New constraints from a Silurian-Lower Devonian volcanogenic massive sulfide (VMS) deposit. *Journal of Geophysical Research: Solid Earth*, 128, e2022JB025020. <https://doi.org/10.1029/2022JB025020>

Received 25 JUN 2022
Accepted 11 FEB 2023

Author Contributions:

Conceptualization: Liang Gao, Qingfei Wang, Jun Deng
Formal analysis: Xinwei Hu, Liang Gao, Qingfei Wang, Jun Deng
Funding acquisition: Liang Gao, Qingfei Wang, Jun Deng
Investigation: Xinwei Hu, Liang Gao, Qingfei Wang, Xiang Sun, Shengchao Xue, Xin Tang
Resources: Liang Gao, Qingfei Wang, Jun Deng
Supervision: Liang Gao, Qingfei Wang, Shihong Zhang, Zhenyu Yang, Jun Deng
Visualization: Xinwei Hu, Liang Gao, Qingfei Wang, Shihong Zhang, Xiang Sun, Shengchao Xue, Xin Tang, Zhenyu Yang, Jun Deng

Abstract The unclear relationship between mineralization, hydrothermal alteration, and rock magnetization in volcanogenic massive sulfide (VMS) deposits limits us from fully understanding the magnetic anomalies and remagnetization process in this type of deposit. We address the issue by conducting systemic paleomagnetic, rock magnetic, petrographic, and X-Ray diffraction studies in the Dapingzhang VMS deposit on the northwestern Indochina Block. Magnetite is the dominant magnetic carrier of hydrothermally altered surrounding rocks and orebody. Magnetite consumption and secondary magnetite formation occurred at different stages and types of hydrothermal alteration. The overall decrease in magnetite concentration from chloritization via silicification to mineralization implies that the magnetite was mostly consumed during hydrothermal alterations. Secondary single domain magnetite, which can carry a remagnetization direction, is proposed to be formed during illitization via the smectite-to-illite transformation. Secondary superparamagnetic magnetite, which was most likely formed during the late stage of chloritization, is unable to carry the stable characteristic remanent magnetization. The site-mean direction of high-temperature and high-coercivity components is $D_g/I_g = 324.5^\circ/43.1^\circ$, and $k_g = 35.1$, with $\alpha_{95} = 6.8^\circ$ before tilt correction, and $D_s/I_s = 316.2^\circ/37.6^\circ$, and $k_s = 16.4$, with $\alpha_{95} = 10.1^\circ$ after tilt correction, with a negative fold test. However, plate reconstruction is limited by the uncertainty of the tilting process following mineralization and the possibility of remagnetization during burial alteration. Therefore, this study provides a mechanism for rock magnetic variation and remagnetization during VMS mineralization.

Plain Language Summary We conducted paleomagnetic, rock magnetic, petrographic, and X-Ray diffraction studies on volcanogenic massive sulfide (VMS) deposit to better understand the interaction between mineralization, hydrothermal alteration, and magnetization in this kind of deposit. Magnetite is the main magnetic carrier of orebodies and surrounding rocks. The overall decrease in magnetite concentration from chloritized samples to orebodies, via silicified samples, explains the low magnetic anomalies in VMS deposits. However, in samples containing a high concentration of chlorite, a significant amount of secondary superparamagnetic magnetite was discovered. Secondary single domain magnetite is ascribed to be formed through the transformation of smectite to illite during hydrothermal alteration, providing an explanation for remagnetization in VMS deposits. Therefore, magnetite consumption and secondary magnetite formation occurred during different types and stages of hydrothermal alteration. The site-mean paleomagnetic direction is calculated, but it cannot be used in plate reconstruction due to the unclear bedding attitudes prior to mineralization and the possibility of remagnetization during burial alteration. This research improves our understanding of the processes of magnetic mineral variation and remagnetization during VMS mineralization.

1. Introduction

Submarine hydrothermal venting is one of the most important metallogenic processes responsible for the formation of economically valuable volcanogenic massive sulfide (VMS) and sedimentary exhalative massive sulfide deposits (Hannington et al., 2005). High-temperature fluids released from mid-ocean ridges, volcanic arcs, and back-arc spreading centers interacting with seawater and surrounding volcanic rocks caused VMS mineralization (Beaulieu & Szafranski, 2020; Caratori Tontini et al., 2012; Fujii et al., 2015). A variety of hydrothermal alterations occur

near submarine volcanic vents during mineralization, such as chloritization, illitization, and silicification (Galley et al., 2007). Low magnetic anomalies are proposed to be induced by the dissolution of magnetite and its transformation into non-magnetic minerals like pyrite during mineralization (e.g., Dekkers et al., 2014; Irving, 1970; Oliva-Urcia et al., 2011; Sztikar et al., 2014; Tivey et al., 2014; S. Wang et al., 2020, 2021; X. Zhao et al., 1998). Prior to VMS mineralization, the increased saturation magnetization during the advanced oxidation stages shows the complexity of magnetization in low-temperature oxidation (D. Wang & Van der Voo, 2004). Maghemitization has been observed and linked to increased coercivity (Cui et al., 1994; D. Wang & Van der Voo, 2004), as well as a decrease in susceptibility (Krása & Herrero-Bervera, 2005) during low-temperature oxidation. On the other hand, the establishment of a well-constrained apparent polar wander path is often limited by widespread remagnetization and a lack of specific strata (Dekkers, 2012; Torsvik & Cocks, 2013; Van der Voo, 2004). Therefore, it is essential to understand different remagnetization mechanisms and to explore new research objects to conduct paleomagnetic studies in areas lacking suitable strata (Butler, 1992; Kent et al., 1987; X. Zhao & Coe, 1984). The ore deposits have proven to be a promising paleomagnetic research object due to the acquisition of remanence during mineralization (Gao et al., 2018, 2019; Symons et al., 1998). These studies have improved our understanding of the interaction between hydrothermal fluids and rocks, as well as how it affects rock magnetization. However, the detailed effects of VMS deposits-related hydrothermal fluids alteration and mineralization on rock magnetization and the acquisition processes of remagnetization direction remain poorly understood.

The Dapingzhang VMS deposit formed in the back-arc environment of the Indochina Block's northwestern margin in the Proto-Tethys (Deng et al., 2014; Metcalfe, 2021). Systematic sampling with various types and degrees of hydrothermal alteration became possible after the ancient VMS deposits rose above the surface of the seawater due to plate tectonics and/or sea-level drop. Paleomagnetism and rock magnetism are combined with X-Ray Diffraction (XRD) analysis to establish the relationship between hydrothermal alteration, mineralization, rock magnetism, and remagnetization. This is supported by electron microscopy analysis. Finally, a model of the spatiotemporal variation of magnetic minerals in VMS deposits is developed.

2. Geological Setting and Sampling

The Tibetan Plateau and surrounding areas are composed of a mosaic of small blocks (Figure 1a; e.g., the Tethyan Himalaya, Lhasa, Qiangtang, Sibumasu, and Indochina blocks), which are thought to have separated from East Gondwana and collided with Eurasia at various times since the late Paleozoic (Advokaat et al., 2018; Deng et al., 2014, 2022; Metcalfe, 2013; G. Zhao et al., 2018). A number of geological processes were involved in the separation, including continental rifting, seafloor spreading, oceanic plate formation and subduction, continental collision, and the opening and closing of the Paleo-Tethys and Neo-Tethys oceans (Deng et al., 2019; Huang et al., 2018; Metcalfe, 2021; Q. Wang et al., 2020, 2022; G. Zhao et al., 2018). The Indochina Block, located on the southeastern edge of the Tibetan Plateau (Figure 1a), was involved in the overall process, from the breakup of East Gondwana to the India-Asian collision (Deng et al., 2021; Gao et al., 2015; S. Li et al., 2017; Z. Yang & Besse, 1993). The Changning-Menglian suture zone separates the Indochina Block from Sibumasu to the west, and the Ailaoshan suture zone separates it from the South China Block to the east (Figure 1a; Q. Wang et al., 2014). Mesozoic sediments cover Early Devonian-Triassic marine deposits in this block (Figure 1b; Lehmann et al., 2013; Metcalfe, 2013).

The Dapingzhang deposit formed during the early stages of East Gondwana breakup and is located in the Paleozoic volcanic arc belt on the northwestern margin of the Indochina Block (Figure 1a; Lehmann et al., 2013). From bottom to top, the strata are the Middle-Upper Silurian and Lower Devonian Daaazi Formation (SDd), the middle Triassic Xiapotou Formation (T₂x), the Dashuijingshan Formation (T₂d), the Choushui Formation (T₂c), the upper Triassic Weiyuan Formation (T₃w), and the middle Jurassic Huakaizuo Formation (J₂h) (Figure 1b; Lehmann et al., 2013; Y. Yang et al., 2008). The Daaazi Formation, which is divided into four members and corresponds to at least three stages of volcanic activity (Figures 1c and 1d; Ru, 2014; Y. Yang et al., 2008). The lowest member (SDd¹) is dominated by quartz keratophyre, rhyolite interbedded with spilite and tuff at the top, supporting the occurrence of sodium-rich volcanism (Figure 1d; Ru, 2014; Zhu et al., 2016). This member has been dated to 413.2 ± 1.7 Ma and 428.28 ± 6.0 Ma (LA-ICP-MS zircon U-Pb dating; Ru, 2014; X. Wang et al., 2021); and 417.3 ± 1.5 Ma, 420.8 ± 1.6 Ma, and 430.7 ± 4.1 Ma (SHRIMP zircon U-Pb dating; Ru, 2014; X. Wang et al., 2021). Gray-green dacite is included in the second member (SDd²) (Figure 1d). The third member (SDd³) is composed of rhyolite and tuff with trace amounts of spilite, pyroclastic material, and siltstone. The

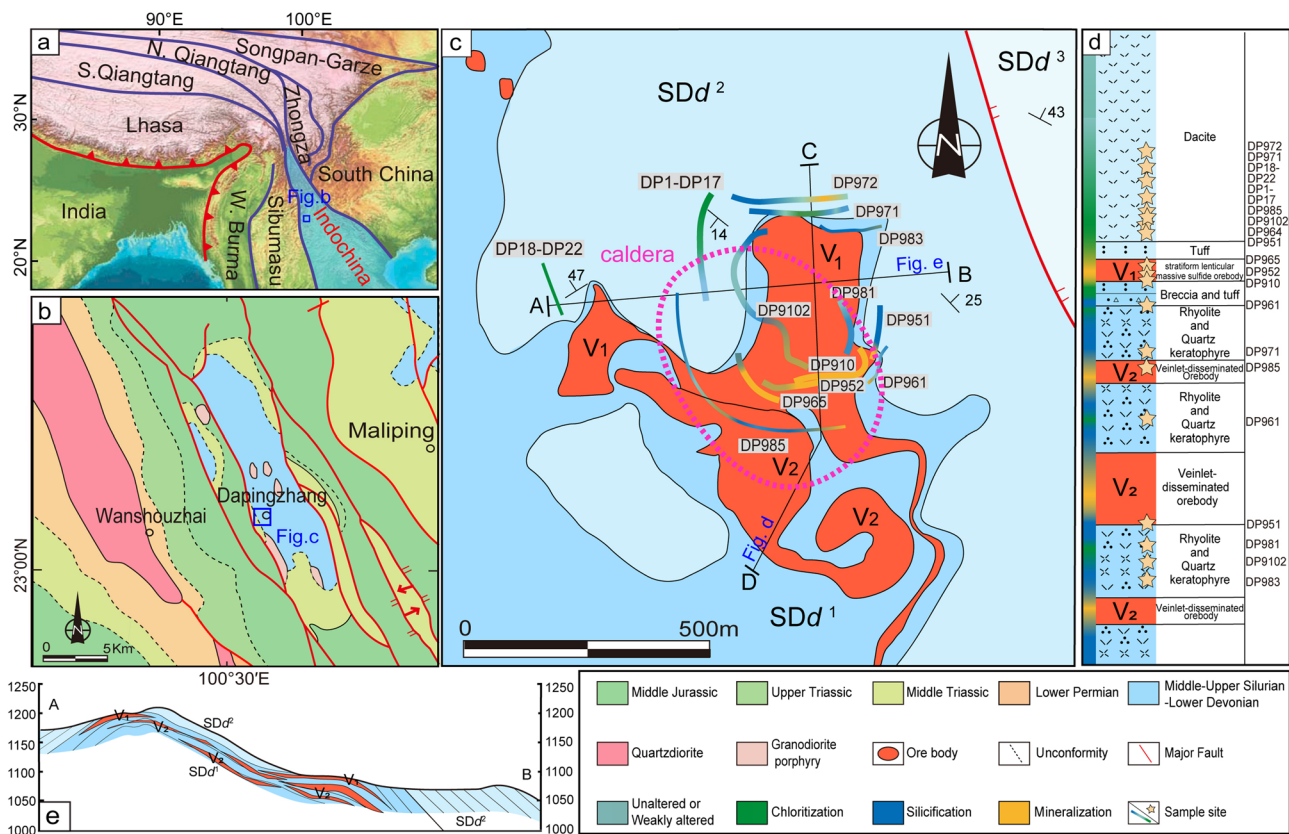


Figure 1. (a–c) Simplified geological map of the Dapingzhang VMS deposit and the surrounding areas (based on the 1:2,00,000 geological map of Yunnan province, and the 1:10,000 geological map of the Dapingzhang deposit); (d) geologic column strata of cross line (C and D) in Figure (c); (e) cross section of (A and B) in Figure (c).

uppermost member (SDd⁴) is made up of keratophyre and tuff, as well as locally formed tuffaceous mudstone and siliceous rocks. The Daozi Formation volcanic rocks are of the calc-alkaline series, with enrichment in large ion lithophile elements and depletion in high-field-strength elements and Light Rare Earth Elements, and are proposed to be formed in an arc-related environment (Hawkesworth et al., 1993; X. Wang et al., 2021). The interaction between volcanic lava and seawater is supported by the high Na₂O content and high Na₂O/K₂O values of felsic volcanic rocks (X. Wang et al., 2021).

The surrounding rocks of the Dapingzhang deposit have been significantly altered by hydrothermal fluids. From the inside of the deposit to the outside, the following processes have been observed: chalcopyritization-pyritization, silicification, brecciation, chloritization-illitization, and carbonatization. Bariteization is only found in isolated massive sulfide orebodies. Meanwhile, the deposit contains V₁ and V₂ orebodies that formed between SDd¹ and SDd² (Figures 1c and 1d; Li & Zhuang, 2000; Ru, 2014). Following the main stage of mineralization, SDd² dacite underwent chloritization-illitization, silicification, and chalcopyritization-pyritization by residual ore-forming fluids (Figure 1d). The V₁ stratiform lenticular massive sulfide orebody is developed in the tuff of the top of SDd¹, with conformable contact with the tuff and dacite of SDd². The main ore-forming minerals are pyrite, sphalerite, chalcopyrite, galena, marcasite, malachite, and limonite (Ru, 2014). The V₂ veinlet-disseminated orebody formed in the sodic rhyolite and volcanic breccias of the upper part of the SDd¹. The main ore-forming minerals include pyrite, sphalerite, chalcopyrite, galena, magnetite, limonite, and sphalerite (Ru, 2014). The V₁ and V₂ orebodies were dated to 410.9 ± 6.0 Ma (Ru, 2014), 437.35 ± 11.2 Ma (Ru, 2014), 428.8 ± 6.1 Ma (W. Li et al., 2010), 442.4 ± 5.6 Ma (W. Li et al., 2010), and 429.0 ± 10.0 Ma (Lehmann et al., 2013) using the Re-Os method on chalcopyrite and molybdenite. Therefore, the isotopic age data support the genetic relation between the orebody and SDd¹, and the main mineralization age is ~415–425 Ma. The δ³⁴S values of chalcopyrite and pyrite range from -2.4 to 2.7‰, indicating that the fluids in the orebody's center are primarily mantle-derived magma mixed with a small amount of seawater (Ru, 2014). Therefore, the alteration types, mineral assemblage and δ³⁴S values reveal typical volcanic rock-hosted VMS formed in a back-arc volcanic environment (Lehmann et al., 2013). The caldera

is almost in the center of the deposit, and the strata surrounding it have varying bedding attitudes (Figure 1c). The original shape of the deposit has been altered due to faulting after mineralization.

A total of 22 sites (203 oriented samples) were collected from two high-resolution sections (DP1-DP17 and DP18-DP22), including the chloritized and silicified dacite (Figure 1d). A portable drill was used to collect 7–10 samples at each site. We also collected 58 unoriented samples from the chloritized-silicified dacite and quartz keratophyre, chalcopyritized-pyritized silicified dacite and quartz keratophyre, and chalcopyrite-pyrite orebody of V_1 and V_2 from places without clear bedding attitudes to constrain the systemic variation in magnetic minerals within the deposit (Figure 1d). No obvious deviation occurred when the magnetic compass was gradually moved close to the rocks. According to the 12th generation of the International Geomagnetic Reference Field, the present-day declination of the sample site is $D = -1.12^\circ$ (Thébault et al., 2015).

3. Scanning Electron Microscope-Energy Dispersive X-Ray Spectroscopy (SEM-EDS)

3.1. Analytical Techniques

Petrographic analyses were performed using a polarizing microscope and a field-emission scanning electron microscope (FESEM) to identify the type and occurrence state of different minerals. Topographic features and compositional differences were revealed using secondary electron imaging detectors and backscattered electron (BSE) images, respectively. Elemental concentrations of $\sim 2 \mu\text{m}$ spots were quantitatively analyzed by energy-dispersive spectroscopy (EDS) attached to the scanning electron microscope, which was used to determine the type of magnetic minerals. The 20 KV accelerating voltage and $\sim 15 \text{ mm}$ working distance were set in Zeiss Supra 55 FESEM and Oxford EDS. These experiments were conducted at the FESEM Laboratory of the China University of Geosciences, Beijing.

3.2. Results

Dacite and quartz keratophyre are intermediate-felsic volcanic rocks with similar mineral and chemical compositions (Ru, 2014; Y. Yang et al., 2008). All collected samples were influenced by varying degrees of chloritization, illitization, and silicification. We classify these samples into four “Groups” based on the predominant hydrothermal alteration types found in each sample: Group A (weakly chloritized rock), Group B (strongly chloritized rock), Group C (weakly silicified rock), and Group D (strongly silicified chalcopyrite-pyrite rock and orebody) (Figure 2).

Chlorite and illite are widely observed in chloritized samples, and gradually replaced albite during the enhancement of chloritization and illitization (Figures 2a and 2b). When the sample is close to orebodies, the type of alteration changes from chloritization to silicification (Figures 2c and 2d). Secondary quartz is found in several strongly chloritized (Figure 2b) and almost all silicified samples (Figures 2c and 2d). Magnetite has been weakly dissolved in weakly chloritized samples (Figure 2a3). Fine-grained magnetite and strongly dissolved hypautomorphic magnetite have been observed in the strongly chloritized samples (Figure 2b3). A large number of monazites distribute around the dissolved magnetite (Figure 2b3). The aggregated fine-grained magnetite formed a spherical shape in strongly chloritized samples (Figures 2b4 and 2b5), which differs from the original hypautomorphic magmatic magnetite (Figures 2a3 and 2b3), suggesting a secondary origin. Pyrite and chalcopyrite are widely observed in orebodies (Figure 2d). The dissolved magnetite is surrounded or replaced by pyrite (Figures 2c3, 2c4, and 2d3), suggesting the strong alteration induced by sulfur-rich reductive fluids. Chalcopyrite formed after pyrite (Figure 2d3). Moreover, the hematite that surrounds the pyrite and quartz was identified, indicating that the hematite formed after the pyrite and quartz (Figure 2d4). Hematite was also observed in the fissures of chalcopyrite (Figure 2d5), indicating that the hematite formed after the chalcopyrite.

4. Powder X-Ray Diffraction (XRD)

4.1. Analytical Techniques

The samples experienced varying degrees of chloritization, illitization, and silicification during mineralization. In order to elucidate the relationship between magnetization and mineralization, it is necessary to provide quantitative constraints on the mineralization-related hydrothermal alteration processes. Therefore, we selected

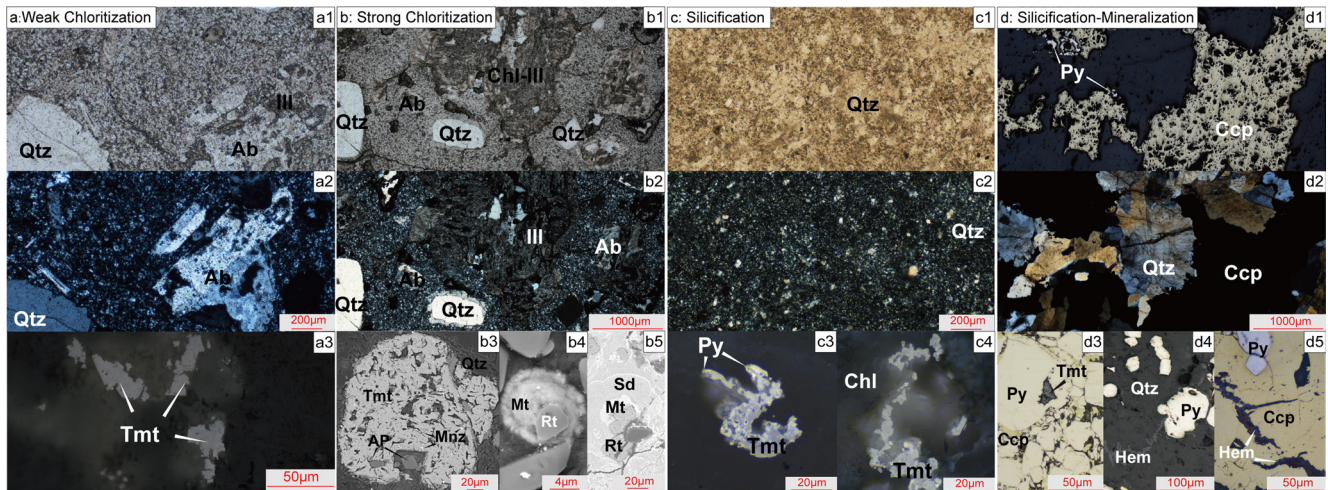


Figure 2. Micrographs of different samples from the Dapingzhang VMS deposit. (a1, a2) Weakly chloritized sample (DP972-1) with good crystal forms of albite and quartz; (a3) dissolution of titanomagnetite in weakly chloritized samples (DP972-1); (b1, b2) a large number of chlorites are identified in strongly chloritized samples (DP19-1); (b3) backscattered electron (BSE) images of dissolved hypautomorphic titanomagnetite in strongly chloritized sample (DP7-3) with apatite and hydrothermal monazite on the edges; (b4, b5) secondary aggregated magnetite is shown in BSE images (DP12-8); (c1, c2) weakly silicified sample (DP981-1); (c3, c4) dissolution of titanomagnetite in weakly silicified sample (DP972-7); (d1, d2) strongly silicified orebody sample (DP985-8) owns a large amount of secondary quartz, porous pyrite and porous chalcopyrite; (d3) chalcopyrite distributed around the pyrite. Dissolved hypautomorphic titanomagnetite are surrounded by pyrite (DP985-12); (d4) hematite veins surround the pyrite and quartz in silicified orebody sample (DP985-8); (d5) hematite veins grow in chalcopyrite fissures (DP952-3); All images except (b3–b5) were taken by polarizing microscope, while the images of (b3–b5) were taken using the scanning electron microscope. From (a to d), the upper images (a1–c1) were taken in plane-polarized light and (d1) was taken in catoptric light, whereas the lower images (a2–d2) were taken in cross-polarized light. The images of magnetic minerals (a3, c3, c4, and d3–d5) were taken in catoptric light. Quartz (Qtz), Albite (Ab), apatite (Ap), pyrite (Py), chalcopyrite (Ccp), chlorite (Chl), illite (Ill), apatite (Ap), titanomagnetite (Tmt), magnetite (Mt), Hematite (Hem), Rutile (Rt), monazite (Mnz), and siderite (Sd).

39 representative powder samples for XRD analysis. The experiments were conducted at the XRD powder crystal laboratory of the China University of Geosciences (Beijing), using a Smart-Lab (9 kW) X-ray diffractometer (Japan), with a Co K α X-ray tube (operated at 40 kV and 200 mA). Data were collected from 3° 2 θ to 70° 2 θ with a step size of 0.02° 2 θ . The divergence slit was 2/3° and the receiving slit was 0.3 mm. Jade 6.0 software (Jade Software Corporation Ltd. Inc., Christchurch, New Zealand) was used for the semi-quantitative analysis of the minerals.

4.2. Results

Quartz, albite, chlorite and illite are identified in almost all samples (Figures 3a–3c; Table S2 in Supporting Information S1). The chlorite content increases from Group A to Group B (Figure 3a). The samples in Group C have the lowest chlorite concentration (Figure 3a). From Group C to Group D, there was an increase in chlorite (Figure 3a) and quartz (Figure 3c) concentrations, indicating that both silicification and chloritization had advanced. The quartz content of the rocks increases from ~50 wt% in weak chloritization to ~90 wt% in silicified orebodies, revealing the silicification enhancement (Figure 3c). Quartz and albite have an apparently negative correlation relationship (Figures 3b and 3c). Illite is mainly found in Groups B and C, with minor concentrations in Groups A and D (Figure 3d). Meanwhile, Group B and Group C can be further divided into two subgroups (x and y) within each group based on the apparent differences in illite concentrations (Figure 3d). The presence of pyrite in silicified orebodies reflects strong mineralization caused by sulfur-rich reductive fluids (Table S2 in Supporting Information S1).

5. Magnetic Mineralogy

5.1. Analytical Techniques

We conducted measurements of low-frequency (χ_{LF} , 470 Hz) and high-frequency (χ_{HF} , 4,700 Hz) magnetic susceptibility, anhysteretic remanent magnetization (ARM), saturation isothermal remanent magnetization (SIRM), backfield isothermal remanent magnetization (IRM), IRM component analysis (Kruiver et al., 2001),

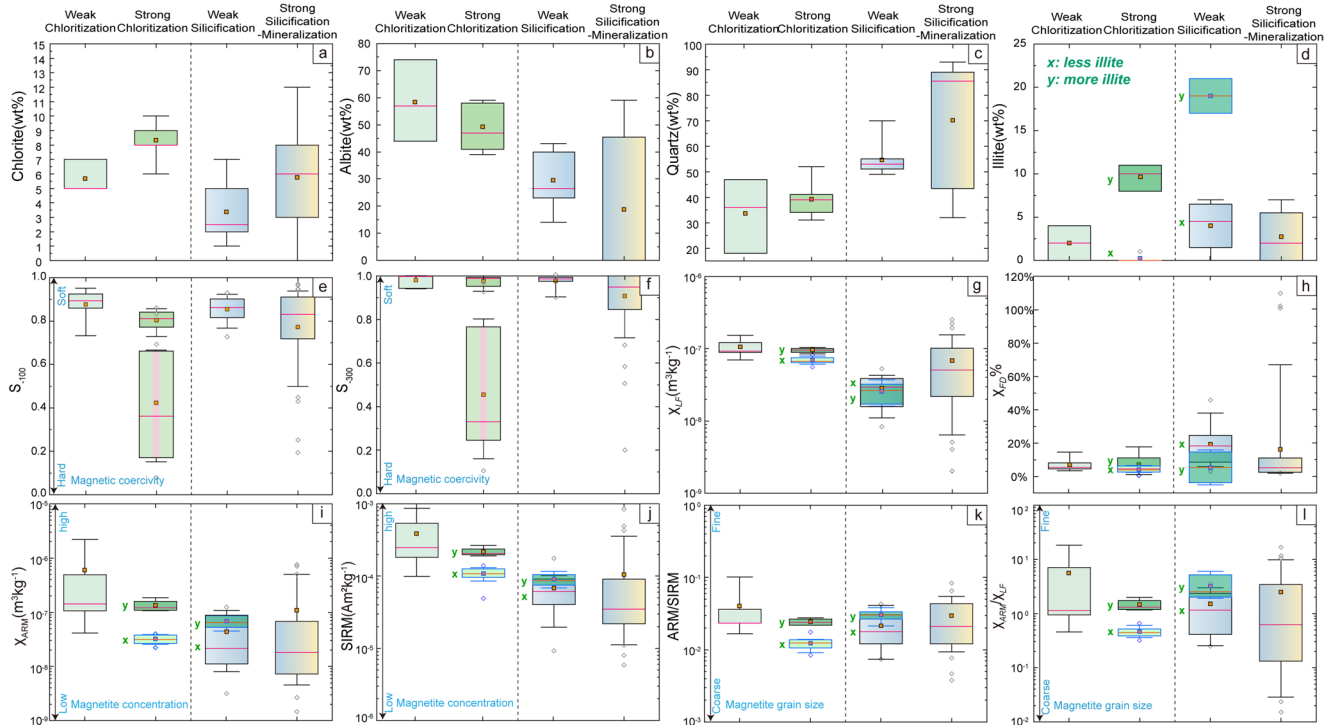


Figure 3. Boxplots of (a) chlorite, (b) albite, (c) quartz, (d) illite, and (e–l) rock magnetic parameters for different samples. The orange dots, purple lines, and gray diamonds show the average, median, and outlier values, respectively. The box and black segments show 1 and 1.5 interquartile ranges. The data can be found in Tables S1 and S2 in Supporting Information S1.

thermal demagnetization of three-component IRMs (Lowrie, 1990), hysteresis loops, and first-order reversal curves (FORCs) on representative samples to identify the magnetic carriers and the relationship between the magnetization process and mineralization. To detect superparamagnetic (SP) magnetite, frequency-dependent susceptibility (χ_{FD}) value was calculated by using the equation $(\chi_{FD}\%) = [(\chi_{LF} - \chi_{HF})/\chi_{LF}] \times 100\%$. $SIRM/\chi_{LF}$, χ_{ARM}/χ_{LF} and $ARM/SIRM$ ratios were calculated to identify the grain size of the magnetic minerals, and χ_{LF} , χ_{ARM} and $SIRM$ are used as indicators of the concentration of magnetic minerals. Magnetic susceptibility and χ_{ARM} are particularly sensitive to SP and single domain (SD) magnetite, respectively (Liu et al., 2004; Maher, 1988). These parameters are commonly used in environmental magnetism studies as rapid indicators of the concentration, grain size, and type of magnetic minerals (Bloemendal et al., 1992; Thompson & Oldfield, 1986; Thompson et al., 1980).

Magnetic susceptibilities (χ_{LF} and χ_{HF}) were measured with a Kappabridge MFK1 (Advanced Geoscience Instruments Company, AGICO). ARM was imparted using a D-2000 AF demagnetizer with a 100 mT (millitesla) alternating field and a 0.05 mT DC field superimposed. SIRM was imparted in a 2.4 T (tesla) DC field and subsequently an IRM was imparted in sequential reverse fields of 0.1 and 0.3 T, along the Z-axis. S_{-100} and S_{-300} were calculated to evaluate the relative amounts of high- and low-coercivity magnetic minerals. S_{-100} and S_{-300} were calculated according to Bloemendal et al. (1992): $S_{-100 \text{ or } -300} = (1 - IRM_{-100 \text{ mT or } -300 \text{ mT}}/SIRM)/2$. The hard, medium and soft magnetization components of orthogonal IRMs were imparted in DC fields of 2.40, 0.40, and 0.12 T, respectively, and thermally demagnetized using an ASC Scientific (ASC) thermal demagnetization (TD) device. ASC pulse magnetizer was used to perform progressive acquisition of IRM up to a maximum field of 2.5 T. Remanent magnetizations were measured with an AGICO JR6 magnetometer. All experiments were conducted at the Paleomagnetism and Environmental Magnetism Laboratory of the China University of Geosciences, Beijing. A vibrating sample magnetometer (Lake Shore model 8604) was used to measure hysteresis loops and FORCs at room temperature in the Key Laboratory of Paleomagnetism and Tectonic Reconstruction of Ministry of Land and Resources. These data were used to determine the saturation magnetization (M_s), the saturation remanent magnetization (M_{rs}), coercive force (B_c) and remanent coercivity (B_{cr}). All of these data were corrected for the paramagnetic content, and FORCinel v 3.06 software was used to plot hysteresis loops and FORC diagrams (Harrison & Feinberg, 2008).

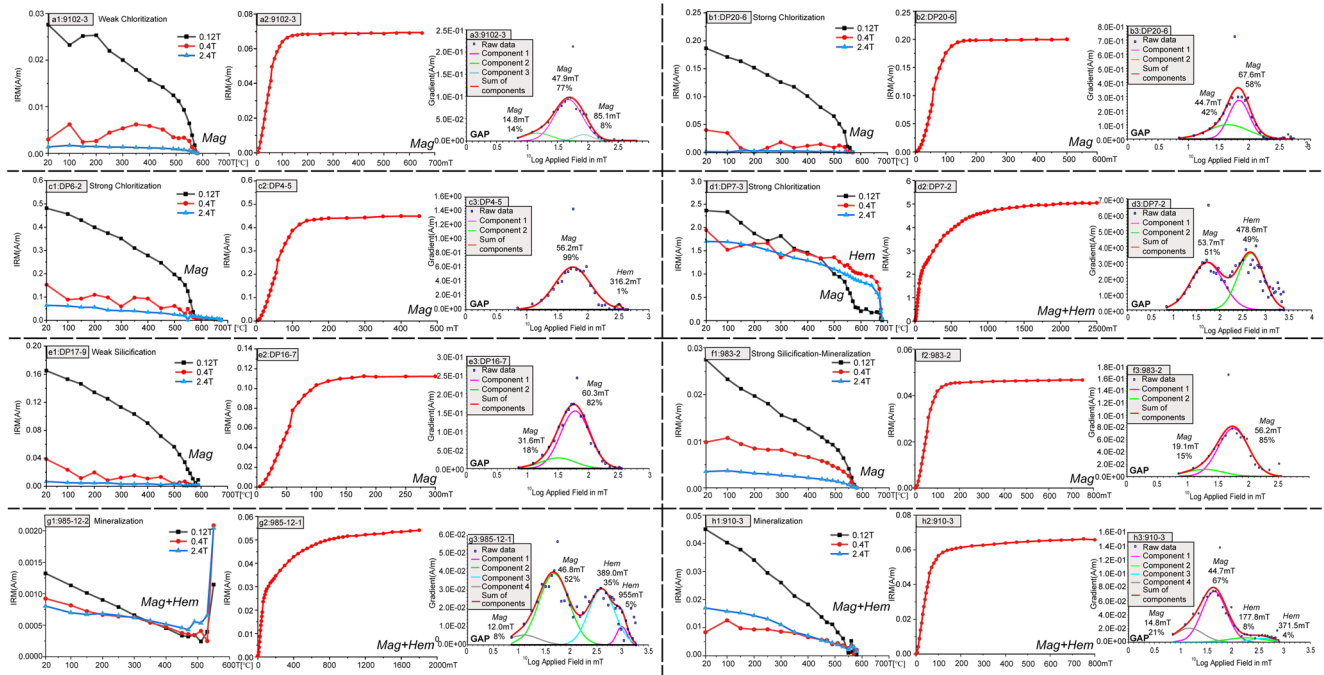


Figure 4. (a1–h1) Thermal demagnetization of three-component IRMs; (a2–h2) isothermal remanent magnetization acquisition curves; (a3–h3) Results of IRM component analysis for representative samples of different alteration types. IRM, Isothermal remanent magnetization; GAP, gradient acquisition plot. Mag, magnetite; Hem, Hematite.

5.2. Results

The rock magnetic parameters of altered dacite and quartz keratophyre are comparable (Table S1 in Supporting Information S1). Based on S_{-100} and S_{-300} values, magnetic minerals with high- and low-coercivity are identified in the samples (Figures 3e and 3f). Because of the significant difference in magnetic coercivity, samples with low and high coercivity were separated in Group B (Figures 3e and 3f). The low-coercivity samples were further used in the discussions of χ_{LF} , χ_{FD} , χ_{ARM} , SIRM, ARM/SIRM, and χ_{ARM}/χ_{LF} variation (Table S1 in Supporting Information S1). Strongly chloritized samples with higher concentration of illite (Group B-subgroup y) have higher χ_{LF} , χ_{ARM} , SIRM, ARM/SIRM, and χ_{ARM}/χ_{LF} than samples with lower concentration of illite (Group B-subgroup x) (Figures 3g, 3i, 3j, 3k and 3l). Weakly silicified samples with higher concentration of illite (Group C-subgroup y) also have higher χ_{ARM} , SIRM, ARM/SIRM, and χ_{ARM}/χ_{LF} than samples with lower concentration of illite (Group C-subgroup x) (Figures 3i–3l). The overall decreased χ_{ARM} and SIRM reveal a reduced magnetite concentration from Group A to Group D (Figures 3i and 3j). The rapid decrease of χ_{ARM} has been observed from weakly (Group A) to strongly chloritized samples (Group B-Subgroup x) (Figure 3i), however the χ_{LF} exhibit a smaller-scale decrease than the χ_{ARM} (Figure 3g). Meanwhile, the χ_{ARM} decreased from Group C to Group D (Figure 3i), opposing the increase in χ_{LF} from Group C to Group D (Figure 3g). Group D samples contain a significant amount of SP magnetite, as evidenced by the higher χ_{LF} (Figure 3g) but lower χ_{FD} (Figure 3h). The lower values of ARM/SIRM in Group B (Figure 3k) indicate a coarser magnetic grain size when compared to Group A. The small-scale variation in magnetite grain size is observed from Group C to Group D (Figure 3k). When compared to the variation of ARM/SIRM (Figure 3k), the χ_{ARM}/χ_{LF} (Figure 3l) show a large-scale decrease from Group C to Group D. This systemic change in magnetite concentration and grain size indicates that magnetic mineralogy variation is controlled by different hydrothermal alteration types.

Different coercivity components could be identified from the results of the thermal demagnetization of three-component IRMs (Lowrie, 1990; Figure 4). The low-coercivity component is unblocked at ~ 550 – 580°C in all samples, indicating the presence of magnetite. Hematite is identified in Groups B and D, with a higher unblocking temperature of $\sim 685^\circ\text{C}$ (Figure 4d1). The IRM experiments show that the saturation of the magnetization for samples 9102-3 (Figure 4a2), DP 20-6 (Figure 4b2), DP4-5 (Figure 4c2), DP16-7 (Figure 4e2), and 983-2 (Figure 4f2) occurred at ~ 200 mT, supporting the dominance of magnetite. For samples DP7-2 (Figure 4d2), 985-12-1 (Figure 4g2), and 910-3 (Figure 4h2), there is an initial rapid increase in the magnetization below ~ 200 mT, but the magnetization is

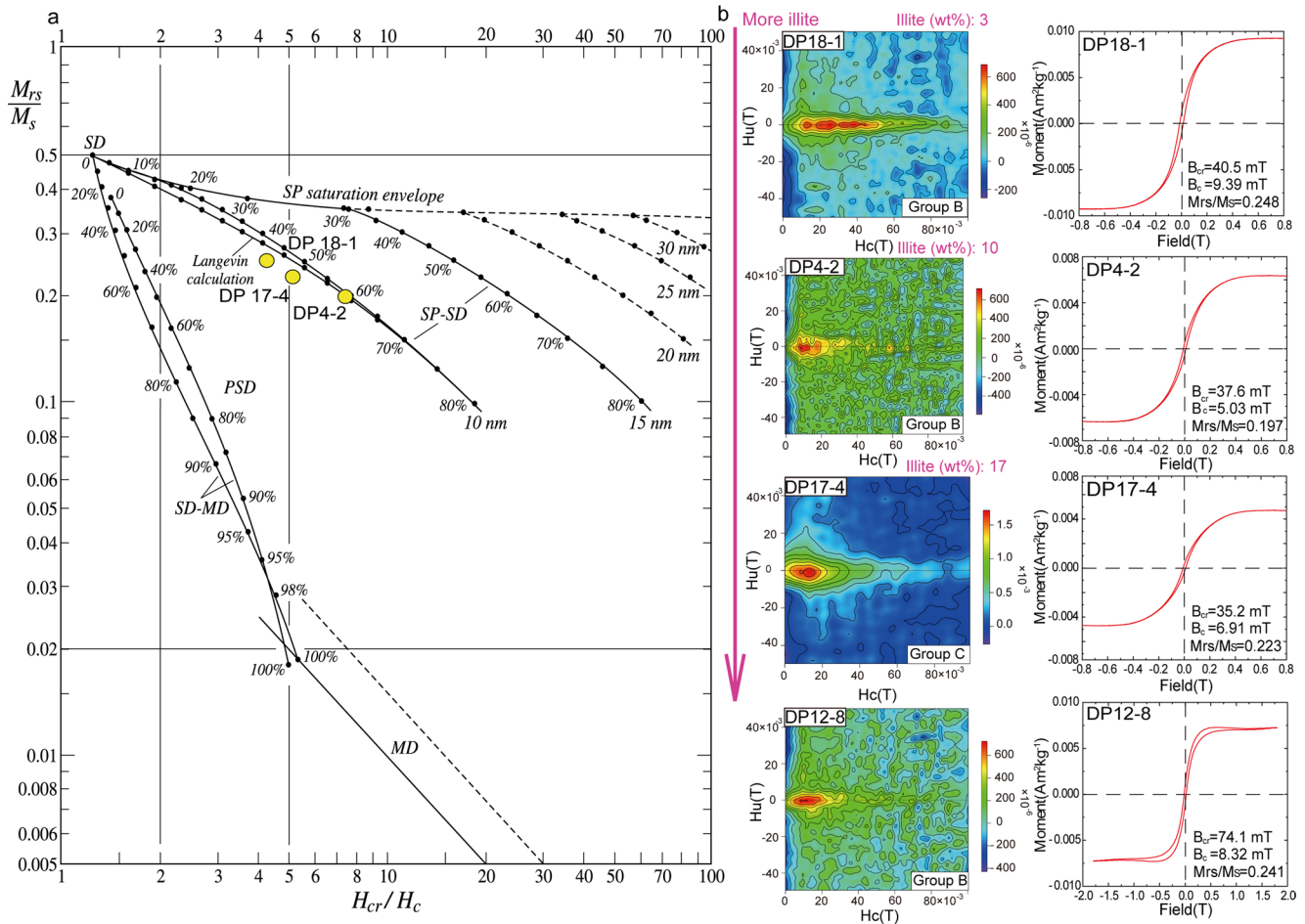


Figure 5. (a) Day plot; (b) first-order reversal curve diagrams and hysteresis loops of representative samples. M_s , saturation magnetization; M_{rs} , saturation remanent magnetization; H_c/B_c , coercive force; H_{cr}/B_{cr} , remanent coercivity; H_u , interaction field.

still unsaturated at ~ 2.5 , ~ 1.8 and ~ 0.8 T, supporting the co-occurrence of both magnetite and hematite. Combined with the Gradient Acquisition Plot (Figures 4a3–4h3), the magnetization of most samples is carried by magnetite. However, hematite is identified in several chloritized and orebody samples. This result is consistent with the lower S_{-300} values of several samples in Groups B and D (Figure 3f), supporting the existence of hematite.

In the Day plot, the representative chloritized and silicified samples (DP 18-1, DP4-2, and DP12-8) are located in the pseudo-single domain region (Figure 5a; Dunlop, 2002; Lanci & Kent, 2003). These samples have a low coercive force (the central H_c is ~ 10 – 20 mT) in FORC diagrams, with a gradual transition from tight distribution of contours along the horizontal axis (DP18-1) to a narrower distribution of contours along the horizontal axis (DP17-4). These characteristics correspond to the existence of noninteracting SD magnetite (DP18-1), weakly interacting SD magnetite (DP4-2), and interacting SD magnetite (DP17-4) (Figure 5b; Roberts et al., 2000). Therefore, the PSD-like magnetite may represent a mixture of SD + SP grains or a mixture of SD + multidomain (MD) grains (Roberts et al., 2000). The corrected hysteresis loops of these three samples are closed within ~ 200 mT, supporting the existence of magnetite (Figure 5b; Dunlop & Özdemir, 1997). Sample DP12-8 has a wasp-waisted hysteresis loop, and the measured loop closes until the field exceeds 1 T, supporting a mixture of magnetite and hematite (Figure 5b; Roberts et al., 1995).

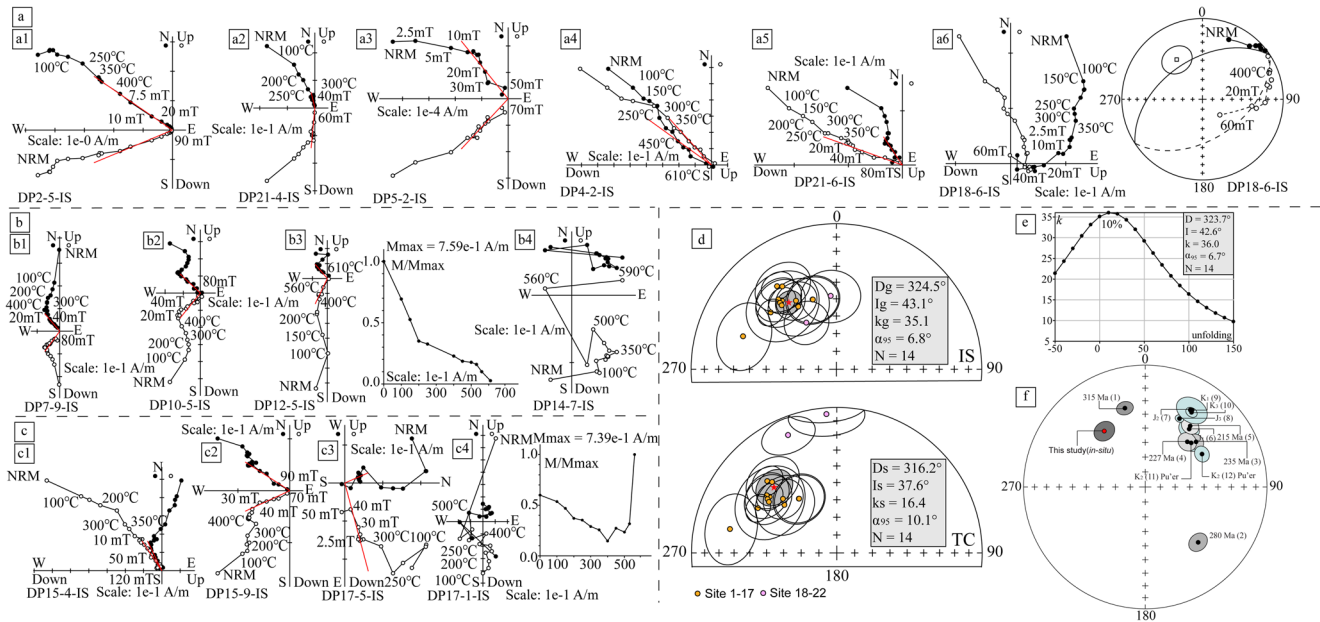


Figure 6. (a–c) Representative Zijderveld diagrams (Zijderveld, 2013) of different sections showing the results of alternating field and thermal demagnetization of the natural remanent magnetization before tilt-correction (in situ, IS); (d) equal-area projections of site-mean directions for the high-temperature and high-coercivity component before (IS) and after tilt-correction (TC). Solid (open) symbols denote lower (upper) hemisphere projections. Red stars represent the average directions, and the shaded circles are the 95% confidence limit. I_g/I_s -inclination in geographic/stratigraphic coordinates; D_g/D_s -declination in geographic/stratigraphic coordinates; α_{95} -radius of the cone at the 95% confidence level about the average of the direction. The images were processed using PaleoMac software (Cogné, 2003); (e) stepwise unfolding result indicating that the characteristic remanent magnetization was acquired at 10% unfolding; (f) equal-area projection for paleomagnetic directions of Indochina Block since ~315 Ma. The numbers of data correspond to Table S5 in Supporting Information S1. K_3 : Upper Cretaceous; K_2 : Middle Cretaceous; K_1 : Lower Cretaceous; J_3 : Upper Jurassic; J_2 : Middle Jurassic; J_1 : Lower Jurassic.

6. Paleomagnetism

6.1. Analytical Techniques

The bedding attitudes of Sites DP 1–DP 22 have been well constrained and therefore suitable for paleomagnetic studies. Samples were cut into cylinders with a diameter of 2.5 cm and a height of 2.2 cm. A TD-48 thermal demagnetizer (magnetic field < 10 nT) and D-2000 alternating-field (AF) demagnetizer were used for thermal and AF demagnetization, using more than 12 steps. An AGICO JR6 magnetometer and 2G Enterprises cryogenic magnetometer were used to measure the remanent magnetization. Both thermal and AF demagnetization were used to isolate the characteristic remanent magnetization (ChRM) of the samples. Principal component analysis (Kirschvink, 1980), the intersection of great circles method (McFadden & McElhinny, 1988) and Fisherian statistics (Fisher, 1953) were used to calculate the component direction and site-mean direction. At least four points were chosen to calculate the component direction. KIRSCH and PMSTAT software (Enkin, 1994) were used to analyze the data.

6.2. Results

The natural remanent magnetization intensities range from 1.95×10^{-2} to 1.35×10^{-4} A/m. The demagnetization curves of representative samples are shown in Figure 6. Although these samples have experienced different degrees of alteration, they show almost identical demagnetization characteristics. One or two magnetization components are isolated during AF or thermal demagnetization. A lower temperature or lower coercivity component is isolated below ~400°C or ~15 mT; a higher temperature component is isolated at ~530–590°C; and a higher coercivity component was isolated at ~50–120 mT. These characteristics indicate that the main magnetic carrier is magnetite. Several samples show unstable demagnetization behavior at high temperatures (Figure 6b4). The remaining samples show an increase in intensity after heating to ~400°C (Figure 6c4), which is probably caused by the oxidation of metal sulfide minerals and the new formation of magnetite. Although hematite is identified in

rock magnetic results, thermal and AF demagnetization results show that the relatively high-coercivity component of these samples are carried mainly by magnetite, with a minor contribution from hematite (Figure 6b3).

The low-temperature component has a northward direction, indicating a viscous magnetization acquired in the present-day geomagnetic field. A ChRM is isolated from 120 samples of 17 sites, among which 18 samples from three sites (DP3, DP9, and DP17) are discarded due to the large A_{95} (Tables S3 and S4 in Supporting Information S1). The samples are dominantly of normal polarity. Reverse polarities are identified using the great circle method; the high-coercivity component move southeastward with a reverse polarity after the removal of the low-temperature component (Figure 6a6). To confirm that the paleosecular variation (PSV) of the samples is fully averaged out, we calculate their PSV (Deenen et al., 2011). $A_{95} = 4.21^\circ$ is located within the range of $A_{95 \text{ max}} = 4.69^\circ$ and $A_{95 \text{ min}} = 1.95^\circ$ ($N = 94$), indicating that these samples have reliably recorded the geomagnetic field. The average site-mean direction for the high-temperature and high-coercivity components for 14 sites is $D_g/I_g = 324.5^\circ/43.1^\circ$, and $k_g = 35.1$, with $\alpha_{95} = 6.8^\circ$ in situ and $D_s/I_s = 316.2^\circ/37.6^\circ$, and $k_s = 16.4$, with $\alpha_{95} = 10.1^\circ$ after tilt-correction (Figure 6d, Table S4 in Supporting Information S1). A syn-tilting diagram gives the optimum grouping at 10% unfolding, with $D/I = 323.7^\circ/42.6^\circ$, and $k = 36.0$, $\alpha_{95} = 6.4^\circ$ (Figure 6e; Watson & Enkin, 1993). Samples with different degrees of alteration have similar in situ site-mean directions (Figure 6d), indicating that the ChRMs of these samples are acquired at almost the same time.

7. Discussion

7.1. Magnetite Consumption During Hydrothermal Alteration and Mineralization

Previous studies have shown that fine-grained magnetite dissolves much more easily than coarse-grained magnetite in both sediments during marine diagenesis (Channell & Hawthorne, 1990) and basalts during hydrothermal alteration (S. Wang et al., 2020). The decrease in χ_{ARM} (Figure 3i) SIRM (Figure 3j), ARM/SIRM (Figure 3k) and $\chi_{\text{ARM}}/\chi_{\text{LF}}$ (Figure 3l) from Group A to Group B suggests that the enhanced chloritization reduced fine-grained magnetite concentration. The magnetite concentration further decreased from weakly (Group C) to strongly (Group D) silicified rocks and orebodies (Figures 3i and 3j). Therefore, the silicified rocks have been experienced stronger magnetite dissolution than chloritized rocks. Meanwhile, the silicification-mineralization consumed both fine- and coarse-grained magnetite as revealed by the small-scale variation in ARM/SIRM from Group C to Group D (Figure 3k). This is different from the chloritization process, which mainly consumed the fine-grained magnetite (Figure 3k). This supports that coarse-grained magnetite is more resistant to the alteration of hydrothermal fluids during chloritization. Therefore, despite the fact that all collected samples were altered to varying degrees, the decrease in magnetite concentration and grain size from weak to strong chloritization and silicification suggests that unaltered surrounding rocks should have a higher concentration of fine-grained magnetite.

7.2. The Neof ormation of SP Magnetite, SD Magnetite and Hematite

The SP magnetite increases χ_{LF} and decreases χ_{FD} but has no effect on ARM and SIRM (Liu et al., 2004; Maher, 1988). Therefore, the existence of SP magnetite can explain why Group D has higher χ_{LF} (Figure 3g) but lower χ_{ARM} (Figure 3i) and SIRM (Figure 3j) when compared to Group C. The positive correlation between the chlorite concentration and χ_{LF} further supports that the χ_{LF} was significantly influenced by chloritization (Figure 7a). The transformation of hornblende, biotite or pyroxene to chlorite can release the Fe ion (Eggleton & Banfield, 1985; Sanderson, 1974), which has the potential to contribute to the formation of secondary SP magnetite. Previous researches have also observed secondary magnetite formation during chloritization (Bergman et al., 2006; Yuguchi et al., 2021). The SD magnetite has been extensively consumed in Group B as evidenced by the abrupt decrease in χ_{ARM} from Group A to Group B-subgroup x (Figures 3i and 8b); Table S1 in Supporting Information S1). However, unlike χ_{ARM} , the χ_{LF} did not show large-scale decrease from Group A to Group B-subgroup x (Figure 3g), which could be attributed to the addition of secondary SP magnetite during chloritization enhancement (Figure 8b). This explains the inconsistent variation in χ_{LF} and χ_{ARM} from Group A to Group B-subgroup x. The existence of SP magnetite also decreases SIRM/ χ_{LF} and $\chi_{\text{ARM}}/\chi_{\text{LF}}$, resulting in data that incorrectly indicates coarse magnetite. This is consistent with our data showing lower SIRM/ χ_{LF} (Table S1 in Supporting Information S1) and $\chi_{\text{ARM}}/\chi_{\text{LF}}$ (Figure 3l) when compared to ARM/SIRM (Figure 3k) in Groups B and D. The decreased χ_{ARM} and SIRM from weak to strong chloritization (Figures 3i and 3j) did not support the formation of significant amount of SD magnetite during chloritization enhancement. Therefore, the overall

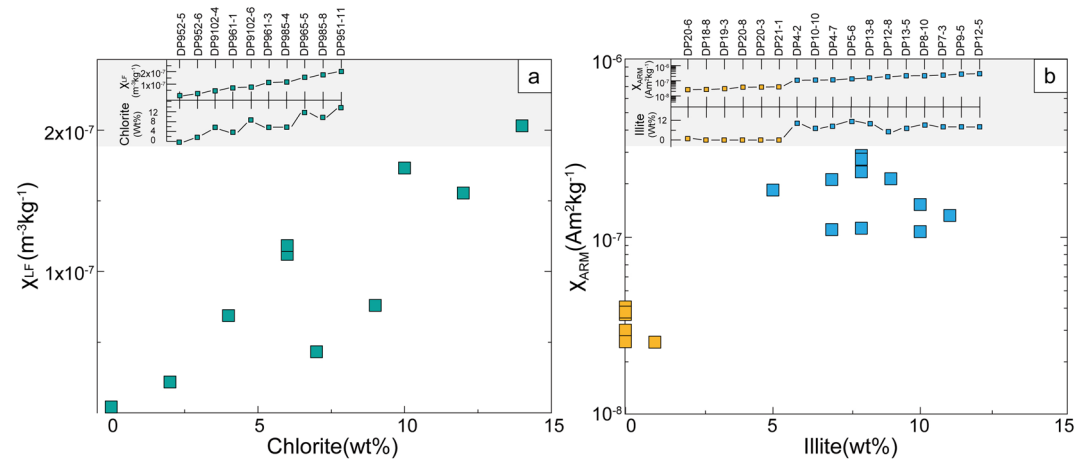


Figure 7. (a) The positive correlation between the amount of chlorite and χ_{LF} ; (b) the positive correlation between the amount of illite and χ_{ARM} . The data can be found in Tables S1 and S2 in Supporting Information S1.

process is deduced to be divided into two substages: the hydrothermal fluids consumed the original fine-grained magmatic SD magnetite first, followed by the secondary SP magnetite formation during the hornblende, biotite or pyroxene transformation to chlorite (Figure 8b).

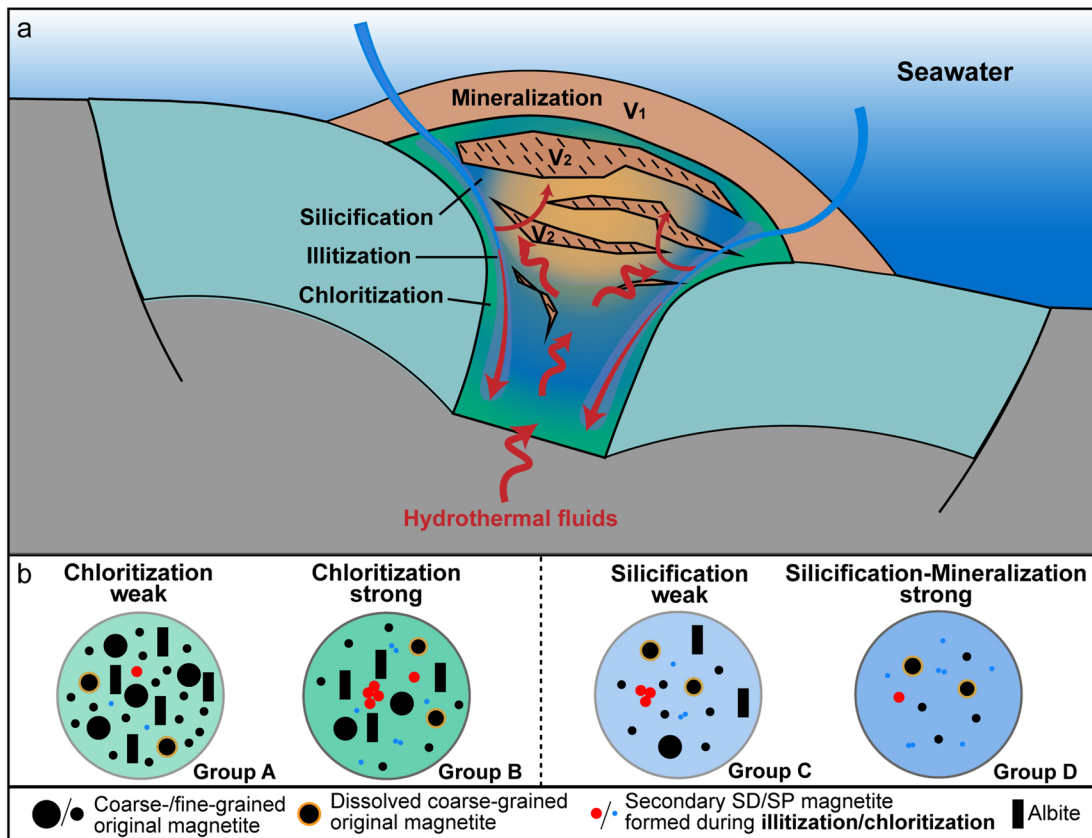


Figure 8. (a) Formation of the Dapingzhang VMS deposit. Mineralization occurred during caldera collapse, and numerous faults and fissures formed near the vents, promoting the infiltration of seawater. The fluids reacted with the wall rock and the segregated brines, carried associated metals to the seafloor, and created Cu-Zn-Au-rich chimneys on the caldera walls and rim. Different hydrothermal alterations occurred during the mineralization (modified from Ru, 2014); (b) the rock magnetic variation of dacite and quartz keratophyre in differential hydrothermal alterations (chloritization, illitization and silicification) and mineralization.

Meanwhile, we observe a synchronous increase in illite and χ_{ARM} (Figure 7b), suggesting that secondary SD magnetite being formed during illitization. The neof ormation of SD magnetite also explains the higher values of χ_{LF} , χ_{ARM} , ARM/SIRM, and $\chi_{\text{ARM}}/\chi_{\text{LF}}$ in samples (subgroup y) with higher concentrations of illite in Groups B and C. FORC diagrams show the gradual transition from noninteracting SD particles (DP18-1) via weakly interacting SD particles (DP4-2) to interacting SD particles (DP17-4) during illitization enhancement (Figure 5b; Roberts et al., 2000). This implies that secondary SD grains are more likely to occur with aggregate configurations, whereas the original magmatic SD grains were not distributed homogeneously. The aggregated magnetite was also observed in strongly chloritized samples (Figure 2b4). This type of magnetite has been proposed to carry remagnetized directions in mafic sill (Bilardello et al., 2018), carbonate (Lu et al., 1990), and shale (Y. Zhang et al., 2016). Meanwhile, previous researches have extensively reported illitization-induced remagnetization via magnetite authigenesis (Gill et al., 2002; Lu et al., 1991; Woods et al., 2002). During diagenesis (Sass et al., 1987), contact metamorphism (Pytte, 1982), and hydrothermal alteration (Cagatay, 1993; Celik et al., 1999; Inoue & Utada, 1983), Fe-rich smectite may become unstable at temperatures above $\sim 75\text{--}100^\circ\text{C}$ and transform to Fe-poor illite via intermediate *I/S* mixed-layered minerals (Altaner & Ylagan, 1997; Bouchet et al., 1988). This process was expected to occur via the reaction of smectite + Al^{3+} + K^+ = illite + Si^{4+} (Celik et al., 1999; Hower et al., 1976). The dissolution of K-feldspars and mica by hydrothermal solutions can provide the potassium (K^+) and aluminum (Al^{3+}) needed for the transformation of smectite to illite (Celik et al., 1999). The release of iron during illitization can promote the formation of secondary magnetite (Hirt et al., 1993), which explains our observation of positive correlation between illite and χ_{ARM} variation (Figure 7b). The lack of smectite in our XRD analysis could be attributed to the small amount of smectite that remained after illitization. But previous researches have widely discovered illite/smectite mixed-layered minerals and the transformation of smectite to illite in hydrothermally altered dacite (Bouchet et al., 1998) and VMS deposits (Cagatay, 1993; Celik et al., 1999). Although the strongly illitized samples of Group C-subgroup y can form a significant amount of secondary SD magnetite, the addition of SD magnetite is still less than the consumption during strong silicification (Figure 8b), as evidenced by the overall decrease in magnetite concentration from Group B to Group C (Figures 3i and 3j). Secondary SD magnetite formation during illitization does not conflict with magnetite consumption during chloritization and silicification as long as these processes are synchronous. Because the authigenic SD magnetite can carry stable ChRM but the SP magnetite cannot, chemical remagnetization most likely occurred during illitization.

Previous studies discovered pyrite, pyrrhotite, chalcopyrite, magnetite, and hematite coexisting in a hydrothermal system (Dekkers et al., 2014; Honsho et al., 2016; X. Zhao et al., 1998). A few samples from Groups B and D contain varying amounts of hematite, which formed after the pyrite and chalcopyrite, as evidenced by petrographic relationships (Figures 2d4 and 2d5). The similar ChRM directions of hematite and magnetite-containing samples exclude the latest formation of hematite (Figure 6). Therefore, the hematite may form in a local oxidizing environment during the late stage of mineralization. Caldera collapse is critical for mineralization in VMS deposits (de Ronde et al., 2019). Following caldera collapse, numerous unevenly distributed faults and fissures appear near the vents, creating seawater infiltration pathways (Anderson et al., 2019; de Ronde et al., 2019). The fluids then interact with the wall rock and segregated brines, transporting metals to the seafloor and forming Cu-Zn-Au-rich chimneys on the caldera walls and rim (de Ronde et al., 2019). The Eu anomaly in this deposit gradually changes from negative to positive from bottom to the top (Ru, 2014), indicating the mixing of oxygen-rich seawater and magma in the deposit. The ore-forming fluid $\delta\text{D}\text{--}\delta^{18}\text{O}$ plots within the mixing zone of oxygen-rich seawater and magma (Ru, 2014). This type of oxygen-rich fluid can create a local oxidizing environment that promotes hematite formation.

7.3. The Uncertainty in Paleomagnetic Plate Reconstruction

Paleomagnetic data of Indochina Block from middle Carboniferous (~ 315 Ma; Yan et al., 2020), Early Middle Permian (~ 280 Ma; Yan et al., 2018), Late Triassic ($\sim 227\text{--}215$ Ma, ~ 205 Ma; Achache & Courtillot, 1985; Yan et al., 2017, 2019; Z. Yang & Besse, 1993), Triassic-Jurassic (Yan et al., 2017), Jurassic (Bhongsuwan & Elming, 2000; Z. Yang & Besse, 1993), Cretaceous (Charusiri et al., 2006; Sato et al., 2007; H. F. Zhang et al., 2012), and Cenozoic (Gao et al., 2015; Sato et al., 2001) have been reported from different studies (Figure 6f; Table S5 in Supporting Information S1). These data provided quantitative constraints on the plate motion and tectonic deformation process of this block. During the middle Carboniferous to Early Middle Permian, the Indochina Block was located in the East Paleo-Tethys Ocean near $\sim 20^\circ\text{S}$, with no significant latitude migration

(Yan et al., 2018, 2020). From the Early Middle Permian to the Late Triassic, this block drifted northward for ~5,000 km, until it reached the southern edge of the Eurasian continent (Yan et al., 2019). Following the collision with Eurasia, the Indochina Block started an internal deformation and lateral extrusion stage (Gao et al., 2015; Sato et al., 2001; Z. Yang & Besse, 1993).

The in situ site-mean direction of the Dapingzhang deposit is different from any reported directions after middle Carboniferous (Figure 6f). Therefore, we cannot preclude the possibility that the original flat strata were destroyed and mainly tilted before the hydrothermal fluids and seawaters interacted with the strata through the faults and fissures because caldera collapse is critical for the mineralization process in VMS deposits (de Ronde et al., 2019). The dip angle for Sites DP2-17 is only 14°, while it is 47° for Sites 18–22 (Figure 1c). These sections are close to each other (~200 m) within the ore district, and the contrasting dip angles can be explained by the local differential displacement of the strata caused by the collapse of the caldera. The 10% optimum grouping during the syn-tilting process can also be explained by caldera collapse–related tilting prior to mineralization and related remagnetization.

In addition, we exclude the possibility of further thermoviscous remagnetization after mineralization for two reasons. First, fluid inclusion studies reveal a maximum mineralization-related temperature of 268°C (Ru, 2014), which is lower than the unblocking temperature of magnetite. Second, typical low-temperature-mineralization-related unstable minerals, such as siderite, chlorite and illite are widely distributed in the samples (Figure 2), implying that high-temperature alteration after mineralization is not possible (Anderson et al., 2019). The deposit was buried to a depth of ~7 km before the Permian, with a burial temperature of ~180–210°C (Ru, 2014), and supported by the K-Ar ages of the spilite (311.8–313.7 Ma) and keratophyre (316.7 Ma) (Zhong et al., 2000). The increased temperature and pressure during burial alteration can cause the release of interstitial brine, and precipitation of secondary metallic minerals, which is supported by the growth of pyrite and chalcopyrite from fine to coarse grain (Ru, 2014). Assume that this deposit was significantly altered during burial metamorphism. In that case, we should observe the variation in geochemical data of metallic minerals from the VMS type to the reworked type deposit. The ³⁴S values of chalcopyrite, pyrite, sphalerite and galena in the deposit, on the other hand, are consistently ~–2.4–2.7‰, which differs from the typical value (~–20.46–5.7‰) of reworked type Cu deposits in the Lanping-Simao Basin (F. Li & Zhuang, 2000; F. Li et al., 1997; Ru, 2014). The lead isotopic compositions of sulfide also support the source of hydrothermal fluids, which are normally related to the upper mantle and lower crust (Ru, 2014).

However, we cannot exclude the possibility of acquiring a remagnetized direction as a result of secondary SD magnetite formation during burial alteration-induced smectite-to-illite conversion. But geochemical data did not support a significant burial alteration in the composition of metallic minerals. Therefore, interstitial brine alteration can be viewed as a continuation of mineralization. In addition, the regular distribution of chloritized rock, silicified rock, chalcopritized-pyritized silicified rock, and chalcopyrite-pyrite orebody from the outside to the inside of the orebody follows the typical alteration pattern in VMS deposits, and did not change after the deposit was buried (Figures 1c and 8a; F. Li & Zhuang, 2000; Ru, 2014; X. Wang et al., 2021; Zhong et al., 2000). The variation in rock magnetic data is well correlated with the various degrees of hydrothermal alteration and mineralization. Therefore, the burial alteration may produce the metallic minerals, improving the accumulation of ores and hydrothermal minerals without significantly altering the basic interaction behavior between mineralization, hydrothermal alteration, and rock magnetization. However, accurate plate reconstruction is still limited by the uncertainty of the tilting process after mineralization.

8. Conclusions

Paleomagnetic, rock magnetic, petrographic, and XRD studies reveal a complex variation process of magnetic minerals during hydrothermal alteration and mineralization in the Dapingzhang VMS deposits. The consumption of original magmatic magnetite and the formation of secondary magnetite occurred at different stages and types of hydrothermal alteration. The overall decreased magnetite concentration and increased proportion of coarse-grained magnetite are observed from weakly chloritized samples to silicified orebodies, supporting a dominated consumption of fine-grained magnetite throughout the process. However, samples with more chlorite and illite contain more SP and SD magnetite, implying that secondary SP and SD grains were formed during chloritization and illitization, respectively. The average site-mean direction for the high-temperature and high-coercivity components is $D_g/I_g = 324.5^\circ/43.1^\circ$, and $k_g = 35.1$, with $\alpha_{95} = 6.8^\circ$ in situ and $D_s/I_s = 316.2^\circ/37.6^\circ$, and $k_s = 16.4$, with $\alpha_{95} = 10.1^\circ$ after tilt-correction. However, the uncertainty of the tilting process after mineralization, as well as the possibility of acquiring a remagnetized direction during burial alteration, limits further plate reconstructions.

In conclusion, our research contributes to a better understanding of the processes of rock magnetism variation and remagnetization during VMS deposit formation.

Data Availability Statement

The data reported in this study can be found in the Supporting Information and the public repository (<https://doi.org/10.6084/m9.figshare.16625077.v4>).

Acknowledgments

This research was supported by the Natural Science Foundation of China (9185217), the National Basic Research Program of China (2015CB452605), the Natural Science Foundation of China (42076223), and the 111 Projects of the Ministry of Science and Technology of China (BP0719021 and B20011). We would like to thank Editor Mark J. Dekkers, Associate Editor Bjarne Almqvist, Eldert Advokaat and Baochun Huang for their valuable suggestions on the manuscript. Special appreciation to the engineers at the Dapingzhang deposit for their support throughout the fieldwork.

References

- Achache, J., & Courtillot, V. (1985). A preliminary upper Triassic paleomagnetic pole for the Khorat plateau (Thailand): Consequences for the accretion of Indochina against Eurasia. *Earth and Planetary Science Letters*, 73(1), 147–157. [https://doi.org/10.1016/0012821X\(85\)90042](https://doi.org/10.1016/0012821X(85)90042)
- Advokaat, E. L., Marshall, N. T., Li, S., Spakman, W., Krijgsman, W., & van Hinsbergen, D. J. (2018). Cenozoic rotation history of Borneo and Sundaland, SE Asia revealed by paleomagnetism, seismic tomography, and kinematic reconstruction. *Tectonics*, 37(8), 2486–2512. <https://doi.org/10.1029/2018TC005010>
- Altaner, S. P., & Ylagan, R. F. (1997). Comparison of structural models of mixed-layer illite/smectite and reaction mechanisms of smectite illitization. *Clays and Clay Minerals*, 45(4), 517–533. <https://doi.org/10.1346/CCMN.1997.0450404>
- Anderson, M. O., Hannington, M. D., McConachy, T. F., Jamieson, J. W., Anders, M., Wienkenjohann, H., et al. (2019). Mineralization and alteration of a modern seafloor massive sulfide deposit hosted in mafic volcanoclastic rocks. *Economic Geology*, 114(5), 857–896. <https://doi.org/10.5382/econgeo.4666>
- Beaulieu, S. E., & Szafranski, K. (2020). Interridge global database of active submarine hydrothermal vent fields. Retrieved from <http://vents-data.interridge.org>
- Bergman, S., Sjöström, H., & Högdahl, K. (2006). Transpressive shear related to arc magmatism: The Paleoproterozoic Storsjön-Edsbyn Deformation Zone, central Sweden. *Tectonics*, 25(1), TC1004. <https://doi.org/10.1029/2005TC001815>
- Bhongsuwan, T., & Elming, S. A. (2000). Research in rock magnetism and palaeomagnetism of recent sediments and Palaeozoic to tertiary rocks in Thailand. Ph.D. thesis (pp. 1–70). Division of Applied Geophysics, Lulea University of Technology.
- Bilardello, D., Callebert, W. C., & Davis, J. R. (2018). Evidence for widespread remagnetizations in South America, case study of the Itararé Group rocks from the state of São Paulo, Brazil. *Frontiers of Earth Science*, 6, 182. <https://doi.org/10.3389/feart.2018.00182>
- Bloemendal, J., King, J. W., Hall, F. R., & Doh, S. J. (1992). Rock magnetism of late Neogene and Pleistocene deep-sea sediments—relationship to sediment source, diagenetic processes, and sediment lithology. *Journal of Geophysical Research*, 97(B4), 4361–4375. <https://doi.org/10.1029/91JB03068>
- Bouchet, A., Proust, D., Meunier, A., & Beaufort, D. (1988). High-charge to low-charge smectite reaction in hydrothermal alteration processes. *Clay Minerals*, 23(2), 133–146. <https://doi.org/10.1180/claymin.1988.023.2.02>
- Butler, R. F. (1992). *Paleomagnetism: Magnetic domains to geologic* (p. 238). Blackwell Scientific Publications.
- Cagatay, M. N. (1993). Hydrothermal alteration associated with volcanogenic massive sulfide deposits; examples from Turkey. *Economic Geology*, 88(3), 606–621. <https://doi.org/10.2113/gsecongeo.88.3.606>
- Caratori Tontini, F., Davy, B., de Ronde, C. E. J., Embley, R. W., Leybourne, M., & Tivey, M. A. (2012). Crustal magnetization of Brothers Volcano, New Zealand, measured by autonomous underwater vehicles: Geophysical expression of a submarine hydrothermal system. *Economic Geology*, 107(8), 1571–1581. <https://doi.org/10.2113/econgeo.107.8.1571>
- Celik, M., Karakaya, N., & Temel, A. (1999). Clay minerals in hydrothermally altered volcanic rocks, Eastern Pontides, Turkey. *Clays and Clay Minerals*, 47(6), 708–717. <https://doi.org/10.1346/CCMN.1999.0470604>
- Channell, J. E. T., & Hawthorne, T. (1990). Progressive dissolution of titanomagnetites at ODP Site 653 (Tyrrhenian Sea). *Earth and Planetary Science Letters*, 96(3–4), 469–480. [https://doi.org/10.1016/0012-821X\(90\)90021-0](https://doi.org/10.1016/0012-821X(90)90021-0)
- Charusiri, P., Imsamut, S., Zhuang, Z., Ampaiwan, T., & Xu, X. (2006). Paleomagnetism of the earliest Cretaceous to early late Cretaceous sandstones, Khorat Group, Northeast Thailand: Implications for tectonic plate movement of the Indochina block. *Gondwana Research*, 9(3), 310–325. <https://doi.org/10.1016/j.gr.2005.11.006>
- Cogné, J. P. (2003). PaleoMac: A Macintosh™ application for treating paleomagnetic data and making plate reconstructions. *Geochemistry, Geophysics, Geosystems*, 4(1), 1007. <https://doi.org/10.1029/2001GC000227>
- Cui, Y., Verosub, K. L., & Roberts, A. P. (1994). The effect of low-temperature oxidation on large multi-domain magnetite. *Geophysical Research Letters*, 21(9), 757–760. <https://doi.org/10.1029/94GL00639>
- Deenen, M. H., Langereis, C. G., van Hinsbergen, D. J., & Biggin, A. J. (2011). Geomagnetic secular variation and the statistics of palaeomagnetic directions. *Geophysical Journal International*, 186(2), 509–520. <https://doi.org/10.1111/j.1365-246X.2011.05050.x>
- Dekkers, M. J. (2012). End-member modelling as an aid to diagnose remagnetization: A brief review. *Geological Society, London, Special Publications*, 371(1), 253–269. <https://doi.org/10.1144/SP371.12>
- Dekkers, M. J., Heslop, D., Herrero-Bervera, E., Acton, G., & Krása, D. (2014). Insights into magmatic processes and hydrothermal alteration of in situ superfast spreading ocean crust at ODP/IODP site 1256 from a cluster analysis of rock magnetic properties. *Geochemistry, Geophysics, Geosystems*, 15(8), 3430–3447. <https://doi.org/10.1002/2014GC005343>
- Deng, J., Wang, Q., Gao, L., He, W., Yang, Z., Zhang, S., et al. (2021). Differential crustal rotation and its control on giant ore clusters along the eastern margin of Tibet. *Geology*, 49(4), 428–432. <https://doi.org/10.1130/G47855.1>
- Deng, J., Wang, Q., Li, G., Li, C., & Wang, C. (2014). Tethys tectonic evolution and its bearing on the distribution of important mineral deposits in the Sanjiang region, SW China. *Gondwana Research*, 26(2), 419–437. <https://doi.org/10.1016/j.gr.2013.08.002>
- Deng, J., Wang, Q., Sun, X., Yang, L., Groves, D. I., Shu, Q., et al. (2022). Tibetan ore deposits: A conjunction of accretionary orogeny and continental collision. *Earth-Science Reviews*, 235, 104245. <https://doi.org/10.1016/j.earscirev.2022.104245>
- Deng, J., Zhai, Y., Mo, X. X., & Wang, Q. (2019). Temporal-spatial distribution of metallic ore deposits in China and their geodynamic settings. *Society of Economic Geologists*, 22, 103–132. <https://doi.org/10.5382/SP.22.04>
- de Ronde, C. E. J., Humphris, S. E., Höfig, T. W., & Reyes, A. G., & the IODP Expedition 376 Scientists. (2019). Critical role of caldera collapse in the formation of seafloor mineralization: The case of Brothers volcano. *Geology*, 47(8), 762–766. <https://doi.org/10.1130/G46047.1>
- Dunlop, D. J. (2002). Theory and application of the day plot (M_s/M_w versus H_c/H_a) 1. Theoretical curves and tests using titanomagnetite data. *Journal of Geophysical Research*, 107(B3), 1–22. <https://doi.org/10.1029/2001JB000486>

- Dunlop, D. J., & Özdemir, Ö. (1997). *Rock magnetism: Fundamentals and frontiers*. Cambridge University press. <https://doi.org/10.1017/CBO9780511612794>
- Eggleton, R. A., & Banfield, J. F. (1985). The alteration of granitic biotite to chlorite. *American Mineralogist*, 70(9–10), 902–910. <https://doi.org/10.1180/minmag.1985.049.354.22>
- Enkin, R. J. (1994). *A computer program package for analysis and presentation of paleomagnetic data* (Vol. 16). Pacific Geoscience Centre. Geological Survey of Canada.
- Fisher, R. A. (1953). Dispersion on a sphere. *Proceedings of the Royal Society of London*, 217(1130), 295–305. <https://doi.org/10.1098/rspa.1953.0064>
- Fujii, M., Okino, K., Honsho, C., Dymont, J., Sztikar, F., & Asada, M. (2015). High-resolution magnetic signature of active hydrothermal systems in the back-arc spreading region of the Southern Mariana Trough. *Journal of Geophysical Research: Solid Earth*, 120(5), 2821–2837. <https://doi.org/10.1002/2014JB011714>
- Galley, A., Hannington, M. D., & Jonasson, I. (2007). Volcanogenic massive sulphide deposits. In W. D. Goodfellow (Ed.), *Mineral deposits of Canada: A synthesis of major deposit-types, district metallogeny, the evolution of geological provinces, and exploration methods: Geological association of Canada* (Vol. 5, pp. 141–161). Mineral Deposits Division, Special Publication.
- Gao, L., Wang, Q., Deng, J., Chen, F., Zhang, S., & Yang, Z. (2019). Magmatic-hydrothermal alteration mechanism for late Mesozoic remagnetization in the South China block. *Journal of Geophysical Research: Solid Earth*, 124(11), 10704–10720. <https://doi.org/10.1029/2019JB018018>
- Gao, L., Wang, Q., Deng, J., Zhang, S., & Yang, Z. (2018). Relationship between orogenic gold mineralization and crustal shearing along Ailaoshan-red river belt, southeastern Tibetan Plateau: New constraint from paleomagnetism. *Geochemistry, Geophysics, Geosystems*, 19(7), 2225–2242. <https://doi.org/10.1029/2018GC007493>
- Gao, L., Yang, Z., Tong, Y., Wang, H., & An, C. (2015). New paleomagnetic studies of Cretaceous and Miocene rocks from Jinggu, western Yunnan, China: Evidence for internal deformation of the Lanping–Simao Terrane. *Journal of Geodynamics*, 89, 39–59. <https://doi.org/10.1016/j.jog.2015.06.004>
- Gill, J. D., Elmore, R. D., & Engel, M. H. (2002). Chemical remagnetization and clay diagenesis: Testing the hypothesis in the Cretaceous sedimentary rocks of northwestern Montana. *Physics and Chemistry of the Earth, Parts A/B/C*, 27(25–31), 1131–1139. [https://doi.org/10.1016/S1474-7065\(02\)00108-0](https://doi.org/10.1016/S1474-7065(02)00108-0)
- Hannington, M. D., de Ronde, C. E. J., & Petersen, S. (2005). Sea-floor tectonics and submarine hydrothermal systems. *Economic Geology 100th Anniversary Volume*, 111–141. <https://doi.org/10.5382/AV100.06>
- Harrison, R. J., & Feinberg, J. M. (2008). FORCinel: An improved algorithm for calculating first-order reversal curve distributions using locally weighted regression smoothing. *Geochemistry, Geophysics, Geosystems*, 9(5), Q05016. <https://doi.org/10.1029/2008GC001987>
- Hawkesworth, C. J., Gallagher, K., Hergt, J. M., & Dermott, F. M. (1993). Trace element fractionation processes in the generation of island arc basalts. *Philosophical transactions of the royal society. A: Mathematical, Physical and Engineering Sciences*, 342(1663), 179–191. <https://doi.org/10.1098/rsta.1993.0013>
- Hirt, A. M., Banin, A., & Gehring, A. U. (1993). Thermal generation of ferromagnetic minerals from iron-enriched smectites. *Geophysical Journal International*, 115(3), 1161–1168. <https://doi.org/10.1111/j.1365-246X.1993.tb01518.x>
- Honsho, C., Yamazaki, T., Ura, T., Okino, K., Morozumi, H., & Ueda, S. (2016). Magnetic anomalies associated with abundant production of pyrrhotite in a sulfide deposit in the Okinawa Trough, Japan. *Geochemistry, Geophysics, Geosystems*, 17, 4413–4424. <https://doi.org/10.1002/2016GC006480>
- Hower, J., Eslinger, E. V., Hower, M. E., & Perry, E. A. (1976). Mechanism of burial metamorphism of argillaceous sediment: 1. Mineralogical and chemical evidence. *The Geological Society of America Bulletin*, 87(5), 725–737. [https://doi.org/10.1130/0016-7606\(1976\)87<725:MOBMOA>2.0.CO;2](https://doi.org/10.1130/0016-7606(1976)87<725:MOBMOA>2.0.CO;2)
- Huang, B., Yan, Y., Piper, J. D., Zhang, D., Yi, Z., Yu, S., & Zhou, T. (2018). Paleomagnetic constraints on the paleogeography of the East Asian blocks during Late Paleozoic and Early Mesozoic times. *Earth-Science Reviews*, 186, 8–36. <https://doi.org/10.1016/j.earscirev.2018.02.004>
- Inoue, A., & Utada, M. (1983). Further investigations of a conversion series of dioctahedral mica/smectites in the Shinzan hydrothermal alteration area, northeast Japan. *Clays and Clay Minerals*, 31(6), 401–412. <https://doi.org/10.1346/CCMN.1983.0310601>
- Irving, E. (1970). The mid-Atlantic ridge at 45°N. XIV. Oxidation and magnetic properties of basalt; review and discussion. *Canadian Journal of Earth Sciences*, 7(6), 1528–1538. <https://doi.org/10.1139/e70-144>
- Kent, D. V., Zeng, X., Wen, Y. Z., & Opdyke, N. D. (1987). Widespread late Mesozoic to recent remagnetization of Paleozoic and lower Triassic sedimentary rocks from South China. *Tectonophysics*, 139(1–2), 133–143. [https://doi.org/10.1016/0040-1951\(87\)90202-2](https://doi.org/10.1016/0040-1951(87)90202-2)
- Kirschvink, J. L. (1980). The least-squares line and plane and the analysis of palaeomagnetic data. *Geophysical Journal of the Royal Astronomical Society*, 62(3), 699–718. <https://doi.org/10.1111/j.1365-246X.1980.tb02601.x>
- Kráša, D., & Herrero-Bervera, E. (2005). Alteration induced changes of magnetic fabric as exemplified by dykes of the Koolau volcanic range. *Earth and Planetary Science Letters*, 240(2), 445–453. <https://doi.org/10.1016/j.epsl.2005.09.028>
- Kruiver, P. P., Dekkers, M. J., & Heslop, D. (2001). Quantification of magnetic coercivity components by the analysis of acquisition curves of isothermal remanent magnetisation. *Earth and Planetary Science Letters*, 189(3–4), 269–276. [https://doi.org/10.1016/S0012-821X\(01\)00367-3](https://doi.org/10.1016/S0012-821X(01)00367-3)
- Lanci, L., & Kent, D. V. (2003). Introduction of thermal activation in forward modeling of SD hysteresis loops and implications for the interpretation of the day diagrams. *Journal of Geophysical Research*, 108(B3), 2142. <https://doi.org/10.1029/2001JB000944>
- Lehmann, B., Zhao, X. F., Zhou, M. F., Du, A. D., Mao, J. W., Zeng, P. S., et al. (2013). Mid-Silurian back-arc spreading at the northeastern margin of Gondwana: The Dapingzhang dacite-hosted massive sulfide deposit, Lancangjiang zone, southwestern Yunnan, China. *Gondwana Research*, 24(2), 648–663. <https://doi.org/10.1016/j.gr.2012.12.018>
- Li, F., Fu, W. M., & Li, L. (1997). The material origin of the regional metallogenesis of Cu deposits in red beds of west Yunnan. *Yunnan Geology*, 16(3), 233–244. (in Chinese with English abstract).
- Li, F., & Zhuang, F. (2000). Geological characteristics and its genesis of Dapingzhang Cu poly-metal deposit in western Yunnan. *Journal of Kunming University of Science and Technology*, 25, 32–36. (in Chinese with English abstract). <https://doi.org/10.16112/j.cnki.53-1223/n.2000.06.010>
- Li, S., Advokaat, E. L., van Hinsbergen, D. J., Koymans, M., Deng, C., & Zhu, R. (2017). Paleomagnetic constraints on the Mesozoic–Cenozoic paleolatitudinal and rotational history of Indochina and South China: Review and updated kinematic reconstruction. *Earth-Science Reviews*, 171, 58–77. <https://doi.org/10.1016/j.earscirev.2017.05.007>
- Li, W., Pan, G., Hou, Z., Mo, X., Wang, L., et al. (2010). *Archipelagic-basin, collision orogenic theory and prospecting techniques along the Nujiang-Lancangjiang-Jinshajiang area in Southwestern China* (pp. 1–491). Geological Publishing House. (In Chinese).
- Liu, Q., Banerjee, S. K., Jackson, M. J., Maher, B. A., Pan, Y., Zhu, R., & Chen, F. (2004). Grain sizes of susceptibility and anhysteretic remanent magnetization carriers in Chinese loess/paleosol sequences. *Journal of Geophysical Research*, 109(B3), B03101. <https://doi.org/10.1029/2003JB002747>

- Lowrie, W. (1990). Identification of ferromagnetic minerals in a rock by coercivity and unblocking temperature properties. *Geophysical Research Letters*, 17(2), 159–162. <https://doi.org/10.1029/GL017i002p00159>
- Lu, G., Marshak, S., & Kent, D. V. (1990). Characteristics of magnetic carriers responsible for Late Paleozoic remagnetization in carbonate strata of the mid-continent, USA. *Earth and Planetary Science Letters*, 99(4), 351–361. [https://doi.org/10.1016/0012-821X\(90\)90139-O](https://doi.org/10.1016/0012-821X(90)90139-O)
- Lu, G., McCabe, C., Hanor, J. S., & Ferrell, R. E. (1991). A genetic link between remagnetization and potassic metasomatism in the Devonian Onondaga Formation, northern Appalachian Basin. *Geophysical Research Letters*, 18(11), 2047–2050. <https://doi.org/10.1029/91GL02665>
- Maher, B. A. (1988). Magnetic properties of some synthetic sub-micron magnetites. *Geophysical Journal International*, 94(1), 83–96. <https://doi.org/10.1111/j.1365-246X.1988.tb03429.x>
- McFadden, P. L., & McElhinny, M. W. (1988). The combined analysis of remagnetization circles and direct observations in paleomagnetism. *Earth and Planetary Science Letters*, 87(1–2), 161–172. [https://doi.org/10.1016/0012-821X\(90\)90132-H](https://doi.org/10.1016/0012-821X(90)90132-H)
- Metcalfe, I. (2013). Gondwana dispersion and Asian accretion: Tectonic and palaeogeographic evolution of eastern Tethys. *Journal of Asian Earth Sciences*, 66, 1–33. <https://doi.org/10.1016/j.jseae.2012.12.020>
- Metcalfe, I. (2021). Multiple Tethyan ocean basins and orogenic belts in Asia. *Gondwana Research*, 100, 87–130. <https://doi.org/10.1016/j.gr.2021.01.012>
- Oliva-Urcia, B., Kontny, A., Vahle, C., & Schleicher, A. M. (2011). Modification of the magnetic mineralogy in basalts due to fluid–rock interactions in a high-temperature geothermal system (Krafla, Iceland). *Geophysical Journal International*, 186(1), 155–174. <https://doi.org/10.1111/j.1365-246X.2011.05029.x>
- Pytte, A. M. (1982). The kinetics of the smectite to illite reaction in contact metamorphic shales. M.A. thesis, Dartmouth College, Hanover, New Hampshire.
- Roberts, A. P., Cui, Y., & Verosub, K. L. (1995). Wasp-waisted hysteresis loops: Mineral magnetic characteristics and discrimination of components in mixed magnetic systems. *Journal of Geophysical Research*, 100(B9), 17909–17924. <https://doi.org/10.1029/95JB00672>
- Roberts, A. P., Pike, C. R., & Verosub, K. L. (2000). First-order reversal curve diagrams: A new tool for characterizing the magnetic properties of natural samples. *Journal of Geophysical Research*, 105(B12), 28461–28475. <https://doi.org/10.1029/2000JB900326>
- Ru, S. (2014). *Mineralization model for the Dapingzhang Cu poly-metallic deposits in Simao Basin*. Kunming University of Science and Technology. (In Chinese with English abstract).
- Sanderson, D. D. (1974). Spatial distribution and origin of magnetite in an intrusive igneous mass. *The Geological Society of America Bulletin*, 85(7), 1183–1188. [https://doi.org/10.1130/0016-7606\(1974\)85<1183:SDA00M>2.0.CO;2](https://doi.org/10.1130/0016-7606(1974)85<1183:SDA00M>2.0.CO;2)
- Sass, B. M., Rosenberg, P. E., & Kittrick, J. A. (1987). The stability of illite/smectite during diagenesis: An experimental study. *Geochimica et Cosmochimica Acta*, 51(8), 2103–2115. [https://doi.org/10.1016/0016-7037\(87\)90259-6](https://doi.org/10.1016/0016-7037(87)90259-6)
- Sato, K., Liu, Y., Wang, Y., Yokoyama, M., Yoshioka, S., Yang, Z., & Otofujii, Y. (2007). Paleomagnetic study of Cretaceous rocks from Pu'er, western Yunnan, China: Evidence of internal deformation of the Indochina block. *Earth and Planetary Science Letters*, 258(1–2), 1–15. <https://doi.org/10.1016/j.epsl.2007.02.043>
- Sato, K., Liu, Y., Zhu, Z., Yang, Z., & Otofujii, Y. (2001). Tertiary paleomagnetic data from northwestern Yunnan, China: Further evidence for large clockwise rotation of the Indochina block and its tectonic implications. *Earth and Planetary Science Letters*, 185(1–2), 185–198. [https://doi.org/10.1016/S0012-821X\(00\)00377-0](https://doi.org/10.1016/S0012-821X(00)00377-0)
- Symons, D. T. A., Lewchuk, M. T., & Sangster, D. F. (1998). Laramide orogenic fluid flow into the Western Canada sedimentary basin; evidence from paleomagnetic dating of the Kicking Horse Mississippi valley-type ore deposit. *Economic Geology*, 93(1), 68–83. <https://doi.org/10.2113/gsecongeo.93.1.68>
- Szitkar, F., Dyment, J., Choi, Y., & Fouquet, Y. (2014). What causes low magnetization at basalt-hosted hydrothermal sites? Insights from inactive site Krasnov (MAR 16°38'N). *Geochemistry, Geophysics, Geosystems*, 15(4), 1441–1451. <https://doi.org/10.1002/2014GC005284>
- Thébault, E., Finlay, C. C., Beggan, C. D., Alken, P., Aubert, J., Barrois, O., et al. (2015). International geomagnetic reference field: The 12th generation. *Earth Planets and Space*, 67(1), 79. <https://doi.org/10.1186/s40623-015-0228-9>
- Thompson, R., & Oldfield, F. (1986). *Environmental magnetism*. Allen & Unwin.
- Thompson, R., Stober, J. C., Turner, G. M., Oldfield, F., Bloemendal, J., Dearing, J. A., & Rummery, T. A. (1980). Environmental applications of magnetic measurements. *Science*, 207(4430), 481–486. <https://doi.org/10.1126/science.207.4430.481>
- Tivey, M. A., Johnson, H. P., Salmi, M. S., & Hutnak, M. (2014). High-resolution near-bottom vector magnetic anomalies over Raven hydrothermal field, Endeavour segment, Juan de Fuca Ridge. *Journal of Geophysical Research: Solid Earth*, 119(10), 7389–7403. <https://doi.org/10.1002/2014JB011223>
- Torsvik, T. H., & Cocks, L. R. M. (2013). Gondwana from top to base in space and time. *Gondwana Research*, 24(3–4), 999–1030. <https://doi.org/10.1016/j.gr.2013.06.012>
- Van der Voo, R. (2004). *Paleomagnetism of the Atlantic, Tethys and Iapetus oceans*. Cambridge University Press.
- Wang, D., & Van der Voo, R. (2004). The hysteresis properties of multidomain magnetite and titanomagnetite/titanomaghemite in mid-ocean ridge basalts. *Earth and Planetary Science Letters*, 220(1–2), 175–184. [https://doi.org/10.1016/S0012-821X\(04\)00052-4](https://doi.org/10.1016/S0012-821X(04)00052-4)
- Wang, Q., Deng, J., Li, C., Li, G., Yu, L., & Qiao, L. (2014). The boundary between the Simao and Yangtze blocks and their locations in Gondwana and Rodinia: Constraints from detrital and inherited zircons. *Gondwana Research*, 26(2), 438–448. <https://doi.org/10.1016/j.gr.2013.10.002>
- Wang, Q., Yang, L., Xu, X., Santosh, M., Wang, Y., Wang, T., et al. (2020). Multi-stage tectonics and metallogeny associated with Phanerozoic evolution of the South China Block: A holistic perspective from the Youjiang Basin. *Earth-Science Reviews*, 211, 103405. <https://doi.org/10.1016/j.earscirev.2020.103405>
- Wang, Q., Yang, L., Zhao, H., Groves, D. I., Weng, W., Xue, S., et al. (2022). Towards a universal model for orogenic gold systems: A perspective based on Chinese examples with geodynamic, temporal, and deposit-scale structural and geochemical diversity. *Earth-Science Reviews*, 224, 103861. <https://doi.org/10.1016/j.earscirev.2021.103861>
- Wang, S., Chang, L., Tao, C., Bilardello, D., Liu, L., & Wu, T. (2021). Seafloor magnetism under hydrothermal alteration: Insights from magnetomineralogy and magnetic properties of the Southwest Indian Ridge basalts. *Journal of Geophysical Research: Solid Earth*, 126(12), e2021JB022646. <https://doi.org/10.1029/2021JB022646>
- Wang, S., Chang, L., Wu, T., & Tao, C. (2020). Progressive dissolution of titanomagnetite in high-temperature hydrothermal vents dramatically reduces magnetization of basaltic ocean crust. *Geophysical Research Letters*, 47(8), e2020GL087578. <https://doi.org/10.1029/2020GL087578>
- Wang, X., Lü, Q., Cao, D., Guo, W., & Peng, R. (2021). Geochronology, geochemistry and zircon Hf-O isotopic composition of ore-bearing volcanic rocks at Dapingzhang VMS Cu-Zn deposit, SW China: Petrogenetic, metallogenic and tectonic implications. *Ore Geology Reviews*, 133, 104040. <https://doi.org/10.1016/j.oregeorev.2021.104040>
- Watson, G. S., & Enkin, R. J. (1993). The fold test in paleomagnetism as a parameter estimation problem. *Geophysical Research Letters*, 20(19), 2135–2137. <https://doi.org/10.1029/93GL01901>

- Woods, S. D., Elmore, R. D., & Engel, M. H. (2002). Paleomagnetic dating of the smectite-to-illite conversion: Testing the hypothesis in Jurassic sedimentary rocks, Skye, Scotland. *Journal of Geophysical Research*, *107*(B5), EPM-2. <https://doi.org/10.1029/2000JB000053>
- Yan, Y., Duan, L., Liang, S., Wang, J., Huang, B., Zheng, W., & Zhang, P. (2020). Paleomagnetic constraint on the carboniferous paleoposition of Indochina and its implications for the evolution of eastern Paleo-Tethys Ocean. *Tectonics*, *39*(7), e2020TC006168. <https://doi.org/10.1029/2020TC006168>
- Yan, Y., Huang, B., Zhang, D., Charusiri, P., & Veeravananakul, A. (2018). Paleomagnetic study on the Permian rocks of the Indochina Block and its implications for paleogeographic configuration and northward drifting of Cathaysia land in the Paleo-Tethys. *Journal of Geophysical Research: Solid Earth*, *123*(6), 4523–4538. <https://doi.org/10.1029/2018JB015511>
- Yan, Y., Huang, B., Zhao, J., Zhang, D., Liu, X., Charusiri, P., & Veeravananakul, A. (2017). Large southward motion and clockwise rotation of Indochina throughout the Mesozoic: Paleomagnetic and detrital zircon U–Pb geochronological constraints. *Earth and Planetary Science Letters*, *459*, 264–278. <https://doi.org/10.1016/j.epsl.2016.11.035>
- Yan, Y., Zhao, Q., Zhang, Y., Huang, B., Zheng, W., & Zhang, P. (2019). Direct paleomagnetic constraint on the closure of Paleo-Tethys and its implications for linking the Tibetan and Southeast Asian Blocks. *Geophysical Research Letters*, *46*(24), 14368–14376. <https://doi.org/10.1029/2019GL085473>
- Yang, Y., Yang, J., Xu, D., & Yang, J. (2008). Mineralization of Dapingzhang massive sulfide copper-polymetallic deposit in Yunnan. *Mineral Deposits*, *27*(02), 230–242. (in Chinese with English abstract).
- Yang, Z., & Besse, J. (1993). Paleomagnetic study of Permian and Mesozoic sedimentary rocks from Northern Thailand supports the extrusion model for Indochina. *Earth and Planetary Science Letters*, *117*(3–4), 525–552. [https://doi.org/10.1016/0012-821X\(93\)90101-E](https://doi.org/10.1016/0012-821X(93)90101-E)
- Yuguchi, T., Matsuki, T., Izumino, Y., Sasao, E., & Nishiyama, T. (2021). Mass transfer associated with chloritization in the hydrothermal alteration process of granitic pluton. *American Mineralogist: Journal of Earth and Planetary Materials*, *106*(7), 1128–1142. <https://doi.org/10.2138/am-2020-7353>
- Zhang, H., Tong, Y., Wang, H., & Yang, Z. (2012). Early Cretaceous paleomagnetic results from Simao of Indochina Block and its tectonic implications. *Acta Geologica Sinica*, *86*(6), 923–939. (in Chinese with English abstract).
- Zhang, Y., Jia, D., Yin, H., Liu, M., Xie, W., Wei, G., & Li, Y. (2016). Remagnetization of lower Silurian black shale and insights into shale gas in the Sichuan Basin, south China. *Journal of Geophysical Research: Solid Earth*, *121*(2), 491–505. <https://doi.org/10.1002/2015JB012502>
- Zhao, G., Wang, Y., Huang, B., Dong, Y., Li, S., Zhang, G., & Yu, S. (2018). Geological reconstructions of the East Asian blocks: From the breakup of Rodinia to the assembly of Pangea. *Earth-Science Reviews*, *186*, 262–286. <https://doi.org/10.1016/j.earscirev.2018.10.003>
- Zhao, X., & Coe, R. S. (1984). Preliminary results of a paleomagnetic study of Paleozoic rock units from eastern China. *Eos Transactions American Geophysical Union*, *65*, 683.
- Zhao, X., Housen, B., Solheid, P., & Xu, W. (1998). Magnetic properties of Leg 158 cores: The origin of remanence and its relation to alteration and mineralization of the active TAG mound. *Proceedings of the Ocean Drilling Program, Scientific Results*, *158*, 337–351. <https://doi.org/10.2973/odp.porc.sr.158.228.1998>
- Zhong, H., Hu, R., Ye, Z., & Tu, G. (2000). Isotope geochronology of Dapingzhang spilite-keratophyre formation in Yunnan Province and its geological significance. *Science in China—Series D: Earth Sciences*, *43*(2), 200–207. <https://doi.org/10.1007/BF02878150>
- Zhu, W., Zhong, H., Yang, Y., & Ren, T. (2016). The origin of the Dapingzhang volcanogenic Cu–Pb–Zn ore deposit, Yunnan province, SW China: Constraints from host rock geochemistry and ore Os–Pb–S–C–O–H isotopes. *Ore Geology Reviews*, *75*, 327–344. <https://doi.org/10.1016/j.oregeorev.2015.12.011>
- Zijderveld, J. D. A. (2013). A. C. Demagnetization of rocks: Analysis of results. *Developments in Solid Earth Geophysics*, *3*, 254–286. <https://doi.org/10.1016/B978-1-4832-2894-5.50049-5>